

SURVEY OF WATER AND AMMONIA IN NEARBY GALAXIES (SWAN): RESOLVED AMMONIA THERMOMETRY, WATER AND METHANOL MASERS IN THE NUCLEAR STARBURST OF NGC 253

MARK GORSKI^{1,2}, JÜRGEN OTT¹, RICHARD RAND², DAVID S. MEIER^{3,1}, EMMANUEL MOMJIAN¹, AND EVA SCHINNERER⁴

¹ National Radio Astronomy Observatory, P.O. Box O, 1003 Lopezville Road, Socorro, NM 87801, USA

² Department of Physics and Astronomy, University of New Mexico, 1919 Lomas Blvd NE, Albuquerque, NM 87131, USA

³ Department of Physics, New Mexico Institute of Mining and Technology, 801 Leroy Place, Socorro, NM 87801, USA

and

⁴ Max-Planck Institut für Astronomie, Königstuhl 17, D-69117 Heidelberg, Germany

ABSTRACT

We present Karl G Jansky Very Large Array molecular line observations of the nearby starburst galaxy NGC 253, from SWAN: "Survey of Water and Ammonia in Nearby galaxies". SWAN is a molecular line survey at centimeter wavelengths designed to reveal the physical conditions of star forming gas over a range of star forming galaxies. NGC 253 has been observed in four 1GHz bands from 21 to 36 GHz at $6'' \sim 100$ pc spatial and 3.5 km s^{-1} spectral resolution. In total we detect 19 transitions from seven molecular and atomic species. We have targeted the metastable inversion transitions of ammonia (NH_3) from (1,1) to (5,5) and the (9,9) line, the 22.2 GHz water (H_2O) ($6_{16} - 5_{23}$) maser, and the 36.1 GHz methanol (CH_3OH) ($4_{-1} - 3_0$) maser. Utilizing NH_3 as a thermometer, we present evidence for uniform heating over the central kpc of NGC 253. The molecular gas is best described by a two kinetic temperature model with a warm 130K and a cooler 57K component. A comparison of these observations with previous ALMA results suggests that the molecular gas is not heated in photon dominated regions or shocks. It is possible that the gas is heated by turbulence or cosmic rays. In the galaxy center we find evidence for NH_3 (3,3) masers. Furthermore we present velocities and luminosities of three water maser features related to the nuclear starburst. We partially resolve CH_3OH masers seen at the edges of the bright molecular emission, which coincides with expanding molecular superbubbles. This suggests that the masers are pumped by weak shocks in the bubble surfaces.

1. INTRODUCTION

Physical descriptions of how the Interstellar Medium (ISM) condenses to form stars, and the resulting feedback from star formation, limit our understanding of galaxy evolution and the star formation history of the universe. Models of galaxy evolution without feedback drastically over predict star formation rates and efficien-

cies. Feedback is necessary to impede star formation otherwise a galaxy reach its peak star formation rate in less than a dynamical time and quickly convert its baryons to stars shortly after (e.g. [Kauffmann et al. 1999](#); [Krumholz et al. 2011](#); [Hopkins et al. 2011](#)). Star formation is largely correlated with the amount of dense, $\geq 10^4 \text{ cm}^{-3}$, molecular gas within a galaxy (e.g. [Gao & Solomon 2004](#)), and in simulations the state of such gas is limited by the resolution of each individual simulation, i.e. subgrid physics (e.g. [Okamoto et al. 2005](#); [Haas et al. 2013](#); [Crain et al. 2015](#)). Consequently, understanding the relationship between star formation, the resulting feedback, and the state of the dense molecular gas is critical to understanding the star formation history of a galaxy.

Feedback in the star forming ISM perturbs molecular

mgorski@unm.edu

jott@nrao.edu

rjr@unm.edu

david.meier@nmt.edu

emomjian@nrao.edu

schinner@mpia.de

gas such that it can no longer collapse and form new stars. Heating from supernovae, stellar winds, and photoionization are examples of the most dominant forms of stellar feedback (e.g. Kauffmann et al. 1999, Hartmann et al. 2001, & Vázquez-Semadeni et al. 2010). One dimensional simulations by Murray et al. (2010) suggest that different mechanisms dominate at different times during the lifetime of star forming Giant Molecular Clouds (GMCs). Furthermore, simulations by Hopkins et al. (2012) and Hopkins et al. (2014) show that these different feedback effects compound in a non-linear way and that no single feedback process dominates the star forming ISM. Additionally, the environment in which star forming material exists may play a critical role in its properties. Therefore, observational constraints are necessary to refine the subgrid physics within the theoretical models on the appropriate scales.

Nearby galaxies provide access to scales of tens of pc where observations can reveal how feedback operates. There are many studies that look at different aspects of feedback. For example in NGC 253 Strickland et al. (2002) and Westmoquette et al. (2011) discuss the X-ray and ionized gas properties of a starburst driven outflow, respectively. Studies of NH_3 , such as those by Ott et al. (2005), Lebrón et al. (2011) and Mangum et al. (2013), reveal heating and cooling of the molecular ISM. In addition, other molecular tracers reveal shocks, Photon Dominated Regions (PDRs), masses, lengths and time scales associated with star formation. (e.g. Meier et al. 2015, Leroy et al. 2015).

The “Survey of Water and Ammonia in Nearby galaxies” (SWAN) is a survey of molecular line tracers at centimeter wavelengths designed to reveal the physical conditions in star forming gas. The sample consists of four star forming galaxies: NGC 253, IC 342, NGC 6946, and NGC 2146, and was chosen to span a range of galaxy types from Milky Way-like to starbursts and an order of magnitude of star formation rates from ($\lesssim 1 \text{ M}_\odot \text{ yr}^{-1}$) to starbursts ($\sim 10 \text{ M}_\odot \text{ yr}^{-1}$). Here we discuss the first results from SWAN focusing on VLA K- and Ka-band observations of NGC 253.

NGC 253 has been studied at many wavelengths: X-ray (e.g. Strickland et al. 2002), optical (e.g. Westmoquette et al. 2011), infrared (e.g. Dale et al. 2009), millimeter (e.g. Bolatto et al. 2013 & Meier et al. 2015), and radio (e.g. Ulvestad & Antonucci 1997). Figure 1 shows a Spitzer $8\mu\text{m}$ image of NGC 253 (Dale et al. 2009). The inset shows the central kpc with 3, 6 and 9σ contours of $\text{NH}_3(3,3)$ emission from our data discussed in Section 3.2.1. We adopt a distance of 3.5 Mpc measured from the tip of the red giant branch (Radburn-Smith et al. 2011) and a systemic velocity of 234 km s^{-1} in the LSRK frame from Whiting (1999). All velocities in this paper will be in the LSRK frame unless

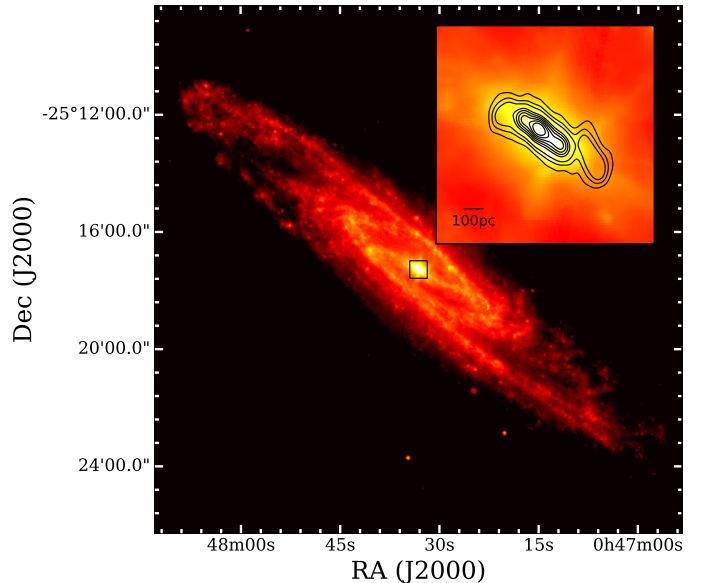


Figure 1. Spitzer IRAC $8.0\mu\text{m}$ image of NGC 253 (Dale et al. 2009). The inset shows the central kpc with $\text{NH}_3(3,3)$ 3, to 30σ contours, with steps of 3σ , showing the dense molecular gas associated with the nuclear starburst. The 3σ contour equates to $4.7 \text{ mJy beam}^{-1} \text{ km s}^{-1}$.

otherwise stated. The disk is inclined at $i \sim 78^\circ$ (Pence 1980). NGC 253 has a total star formation rate (SFR) of $\sim 5.9 \text{ M}_\odot \text{ yr}^{-1}$ of which approximately half is concentrated into the central kpc (McCormick et al. 2013). The starburst is driving a massive molecular outflow, with a mass-loss rate estimated at $9 \text{ M}_\odot \text{ yr}^{-1}$, that is thought to be starving the current star forming event (Bolatto et al. 2013). The outflow is also seen in X-rays (Strickland et al. 2002) and $\text{H}\alpha$ (Watson et al. 1996). Sakamoto et al. (2006) found evidence for two expanding molecular superbubbles within the central kpc with kinetic energies of order $\sim 10^{46} \text{ J}$. Ott et al. (2005) and Bolatto et al. (2013) found several smaller molecular superbubbles in the same region. Bolatto et al. (2013) suggest that superbubbles and supernovae from the starburst drive the wind, whereas Westmoquette et al. (2011) favor a cosmic ray driven wind on the larger scales with a small contribution from the starburst in the center, with the molecular gas in the center responsible for collimating the outflow.

Centimeter and millimeter wavelength spectra of galaxies provide access to diagnostically important molecular tracers. The molecular gas is often well traced by CO, however more complex molecules can provide better tracers of gas properties such as temperature and density, and can be used to trace specific conditions such as PDRs and shocks (e.g. Fuente et al. 1993, García-Burillo et al. 2000, Meier & Turner 2005, and Meier et

al. 2015). This study will focus on the metastable transitions ($J=K$) (1,1) to (5,5) and (9,9) of NH_3 , the 22 GHz $\text{H}_2\text{O}(6_{16}-5_{23})$ maser, and the 36 GHz $\text{CH}_3\text{OH}(4_{14}-3_{03})$ maser. We will use a combined analysis of these lines to expose the processes that dominate the central kpc of NGC 253.

The NH_3 molecule generally works well as a temperature tracer of the molecular gas. The tetrahedral structure of NH_3 makes it a symmetric top, meaning the energy states are described by the rotation angular momentum quantum number J and the projection along the symmetry axis K . The $J=K$ states, called metastable states, are long lived compared to $J>K$ states, and population exchanges between K ladders are forbidden except by collisions. Therefore when NH_3 is collisionally excited (critical density $n_{\text{H}_2} \gtrsim 10^3 \text{ cm}^{-3}$) the K ladders are expected to be populated in accordance with the kinetic temperature of the gas. As a result, measurements of the relative intensities of metastable states act as probes of the rotation temperature of the gas (e.g. Ho & Townes 1983, Walmsley & Ungerechts 1983, Lebrón et al. 2011, Ott et al. 2005, Ott et al. 2011, and Mangum et al. 2013).

The $\text{NH}_3(3,3)$ state can be a maser transition (Walmsley & Ungerechts 1983), but it is less well studied than other masers. In the Galaxy there is a weak association of $\text{NH}_3(3,3)$ masers with dense gas in star forming regions (e.g. Wilson & Mauersberger 1990, Mills & Morris 2013, and Goddi et al. 2015). Here we will use metastable transitions of NH_3 to understand the heating and cooling balance of the dense molecular ISM in NGC 253.

The H_2O and CH_3OH masers provide a unique opportunity to probe star forming environments. The H_2O line requires gas densities $> 10^7 \text{ cm}^{-3}$ and kinetic temperatures $> 300 \text{ K}$ to mase (e.g. Tarchi 2012). In the Galaxy these masers are typically found in shocked regions around Young Stellar Objects (YSOs) and Asymptotic Giant Branch (AGB) stars (e.g. Palagi et al. 1993) and may be used to identify regions of hot, dense, and/or shocked gas. This is in addition to precisely tracing kinematics of stellar winds (e.g. Goddi & Moscadelli 2006), and accretion disks (e.g. Peck et al. 2003; Lo 2005; Reid et al. 2009).

Class I (collisionally pumped) and II (radiatively pumped) CH_3OH masers are found in high mass star forming regions (e.g. Ellingsen et al. 2012) and supernova remnants (e.g. McEwen et al. 2014) in the Galaxy. The Class I masers trace shocks and gas densities $> 10^4 \text{ cm}^{-3}$ (Pratap et al. 2008). The 36.2 GHz CH_3OH line studied here is a Class I type maser. We will mostly use these masers as signposts of shocked material.

In §2 we describe the observational setup. In §3 we re-

port our measurements of the NH_3 , H_2O , and CH_3OH lines in addition to a brief description of the continuum and the H56 α Radio Recombination Line (RRL). In §4 we discuss the derivation of temperatures across the molecular bar, the relevance of the H_2O masers to the outflow, the significance of the CH_3OH masers, and a comparison with previous ALMA millimeter molecular lines. Lastly, we summarize our findings in §5.

2. OBSERVATIONS AND DATA REDUCTION

We observed NGC 253 with the 18-26.5 GHz and 26.5-40 GHz (K- and Ka-bands) receivers of the Karl G. Jansky Very Large Array (VLA)¹ (project code: 13A-375). The K-band observations were carried out on 2013 May 11. The Ka-band observations were split into two sessions: 2013 May 23 and 2013 May 26. The VLA was in the DnC hybrid configuration for all these observations. This configuration delivers a rounder beam for low declination sources because the north arm is in the more extended C configuration, while the east and west arms are in D configuration. The received signal is sampled at each antenna using the 8-bit samplers. These provide two 1 GHz baseband pairs with both right and left hand circular polarizations. The correlator was set up to divide each baseband into 8 sub-bands each with 512 channels resulting in a channel width of 250kHz. This yields a velocity resolution ranging from 3.0 to 3.3 km s^{-1} for the K-band, and 2.0 to 2.7 km s^{-1} for the Ka-band observations. The baseband pairs were centered at 21.8 GHz and 24.1 GHz in K-band, 27.1 GHz and 36.4 GHz in Ka-band. They will be referred to as the 22 GHz, 24 GHz, 27 GHz, and 36 GHz basebands, respectively. These were chosen to include the metastable NH_3 transitions from (1,1) with rest frequency 26.6946 GHz, to (5,5) at 24.5330 GHz, as well as (9,9) at 27.4779 GHz, the $\text{H}_2\text{O}(6_{16}-5_{23})$ maser line at 22.2351 GHz, and the $\text{CH}_3\text{OH}(4_{14}-3_{03})$ transition at 36.1693 GHz. All of the detected lines and their rest frequencies are listed in Table 1. The on source time for the K-band and Ka-band observations was 4.4 hours and 3.6 hours, respectively. We used 3C48 as the flux density calibrator Perley & Butler (2013), J2253+1608 as the bandpass calibrator, and J0025-2602 as the complex gain calibrator in all observations. We alternated between 10 minute intervals on NGC 253 and 1.5 minute intervals on the complex gain calibrator.

The data were reduced in the Common Astronomy Software Applications (CASA) package version 4.2.2 (McMullin et al. 2007). At the adopted distance of 3.5

¹ The National Radio Astronomy Observatory is a facility of the National Science Foundation operated under cooperative agreement by Associated Universities, Inc.

Mpc the linear scale is ~ 17 pc per arcsecond. The half power primary beam widths of the VLA for the K- and Ka-bands are $2.1'$ (~ 2 kpc) and $1.5'$ (~ 1.5 kpc) respectively. All data cubes were gridded with $0.25''$ pixels, mapped using natural weighting, CLEANed to $\sim 3\sigma$ rms noise, and are regridded to a common velocity resolution of 3.5 km s^{-1} . Continuum subtraction was performed in the UV domain. For the 24 GHz baseband, several baselines were flagged for being noisy yielding a slightly larger synthesized beam than the 22GHz baseband. The resulting image cubes are then smoothed to a common synthesized beam of $6'' \times 4''$ (Position Angle: 3.00°). The common resolution cubes are used for consistency for all the observed lines. The resulting rms noise values in the K-band and Ka-band image cubes are $0.5 \text{ mJy beam}^{-1}$ and 1 mJy beam^{-1} in a 3.5 km s^{-1} channel, respectively. The maser lines of H_2O , CH_3OH , and $\text{NH}_3(3,3)$ have also been imaged with $0.25''$ pixels and Briggs (robust=0) weighting, yielding a synthesized beam of $4'' \times 3''$ for H_2O and $\text{NH}_3(3,3)$ and $2'' \times 1''$ for CH_3OH , to better constrain the locations of masing material. The rms noise in the K-band and Ka-band Briggs weighted image cubes are $1.5 \text{ mJy beam}^{-1}$ and $3.1 \text{ mJy beam}^{-1}$ in a 3.5 km s^{-1} channel, respectively. A super-resolved cube was constructed for the H_2O maser data. This was done by deconvolving a dirty image cube then convolving the CLEAN components with a $1''$ round beam. This super-resolved image cube is used to emphasize structures seen in the CLEAN components that are difficult to discern in the regularly resolved image cubes. No quantitative measurements are made with the super-resolved cube.

Table 1. Detected Molecular and Atomic Transitions

Transition	Rest Frequency (GHz)
c-C ₃ H ₂ (2 ₂₀ -2 ₁₁)	21.5874
H₂O(6₁₆ - 5₂₃)	22.2351
H66 α	22.3642
H64 α	24.5099
NH₃ (1,1)	23.6945
NH₃ (2,2)	23.7226
NH₃ (3,3)	23.8701
NH₃ (4,4)	24.1394
NH₃ (5,5)	24.5330
H62 α	26.9392
c-C ₃ H ₂ (3 ₃₀ -3 ₂₁)	27.0843
HC ₃ N (3-2)	27.2944
NH₃ (9,9)	27.4779
CH₃OH (4₋₁ - 3₃)	36.1693

Table 1 continued

Table 1 (*continued*)

Transition	Rest Frequency (GHz)
HC ₃ N (4-3)	36.3924
H56 α	36.4663
CH ₃ CN (2-1)	36.7956

NOTE—Molecules selected for this paper’s analysis are shown in bold face text

3. RESULTS

The full continuum subtracted spectra of our K- and Ka-band observations are presented in Figure 2. We have identified 17 transitions from seven different molecular or atomic species shown in Table 1. Lines were identified by searching the common resolution data cubes with a pixel sized beam. We set conservative conditions for a detection at a peak flux of $>1.5 \text{ mJy beam}^{-1} \text{ channel}^{-1}$ for K-band and $>3.0 \text{ mJy beam}^{-1} \text{ channel}^{-1}$ for Ka-band, and a FWHM of $\gtrsim 30 \text{ km s}^{-1}$ for thermal lines. For known maser transitions single channels above 6σ are considered detections.

3.1. Continuum Emission and Radio Recombination Lines

The radio continuum emission from NGC 253 is resolved in all four basebands (Figure 3). Images were made selecting only line free channels. The flux density measured in the 24 GHz baseband is $550 \pm 30 \text{ mJy}$. This agrees with the value of $520 \pm 52 \text{ mJy}$ from Ott et al. (2005). The 36 GHz flux density measures $350 \pm 40 \text{ mJy}$ in close agreement with the value of 330 mJy at 32 GHz measured by Kepley et al. (2011). The other continuum flux density measurements are $470 \pm 20 \text{ mJy}$ and $370 \pm 40 \text{ mJy}$ for the 22 GHz and 27 GHz basebands, respectively. The spectral index derived from the K-band basebands is -1.8 ± 0.5 and for Ka-band 0.2 ± 0.4 . The measurements suggest the continuum goes through a minimum between the 24 GHz and 27 GHz basebands. The H56 α transition is the strongest radio recombination line (RRL) we detect. Figure 4 shows the relationship between the Hubble (HST) H α (Watson et al. 1996), H56 α , Pa α (Alonso-Herrero et al. 2003), and the 36 GHz continuum emission. We treat the H α as a tracer of the outflow with heavy dust obscuration, Pa α as a partially obscured star formation tracer and RRL as an unobscured star formation tracer.

3.2. Molecular Emission Lines

Our analysis from here on will focus only on NH_3 , H_2O , and CH_3OH . These transitions are shown in bold

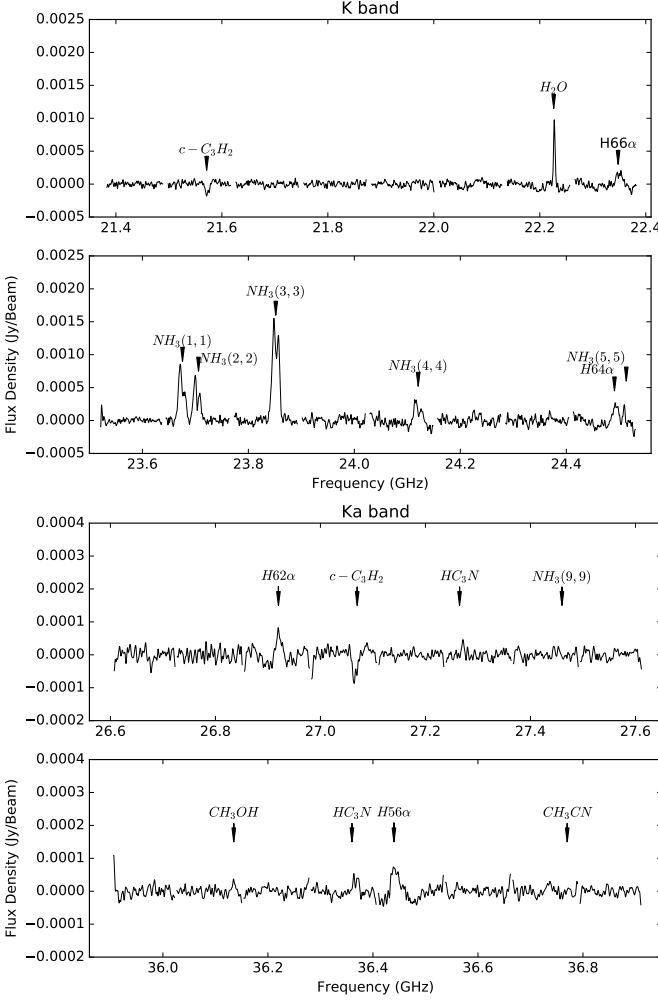


Figure 2. The observed spectrum from K-band and Ka-band. The spectrum was extracted from a $40'' \times 25''$ box centered at RA: $00^h 47^m 33.12^s$ DEC: $-25^\circ 17' 19.33''$ and Hanning smoothed with a window of 21 channels. Each box shows the selected 1GHz basebands with frequency on the X-axis and flux density on the Y-axis. Detected molecular and atomic species are identified with black arrows.

text in Table 1. Intensity and peak flux maps are shown in Figure 5. Spectra have been extracted from the naturally weighted, smoothed cubes from the pixels at the locations marked by crosses (Figure 5) and are shown in Figures 6, 7, and 8. These locations were selected from the spatial peaks in the peak flux maps shown, or for spectrally unique characteristics. For example, W2 is not a spatial peak in the peak flux map but was selected for a spectral component discussed in Section 3.2.2. The continuum peak is labeled C1, and identifies the starburst center. The NH_3 locations are labeled A1-A7. We use the $\text{NH}_3(3,3)$ line to select a representative sample of locations across NGC 253 because it is the strongest observed NH_3 transition. Locations for H_2O and CH_3OH are labeled with W and M, respectively.

3.2.1. NH_3 Inversion Lines

The observed NH_3 emission spans an elongated structure ~ 1 kpc in length about the continuum peak. The northeast (NE) side of the continuum peak contains three $\text{NH}_3(3,3)$ spatial peaks (A1, A2 & A3), which are blueshifted from the systemic velocity with observed velocities ranging from $\sim 160 \text{ km s}^{-1}$ to 200 km s^{-1} . The southwest (SW) side of the continuum peak contains four $\text{NH}_3(3,3)$ peaks (A4, A5, A6, & A7), which are redshifted from systemic with velocities ranging from $\sim 280 \text{ km s}^{-1}$ to 320 km s^{-1} . (Figure 5). The peaks A1, A2, & A3 can be cross-identified with in regions F, E, and D from Ott et al. (2005) and A4, A5, A6 and A7 are analogous to C, B, and A. It should be noted that this is not a one to one mapping as we have a smaller beam than the superresolved cube used in Ott et al. (2005). The NH_3 spectra from each pixel are shown in Figure 6. We detect inversion transitions $\text{NH}_3(1,1)$ to $(5,5)$ at all locations. In addition the $\text{NH}_3(9,9)$ line is weakly detected at site A3 (spectrum not shown). At the continuum peak all the NH_3 transitions are seen in absorption with the exception of $\text{NH}_3(3,3)$. Single Gaussians were fitted to the spectrum extracted from each location, from which we extract the integrated flux, peak flux, FWHM, and the line center, from the individual pixels marked in Figure 5. The properties of the metastable transitions, $\text{NH}_3(1,1)$ to $(5,5)$, for A1-A7 are listed in Table 2 and C1 in Table 3. The weakly detected $\text{NH}_3(9,9)$ fit results are listed in Table 4. We do not see the NH_3 metastable inversion hyperfine transitions ($J=K$, $\Delta F = 1$) as the lines are likely weak and broad enough to be smeared out.

A1, A5 and A6 FWHMs are a few tens of km s^{-1} wider than the other locations. These three sites are located on the edges of superbubbles (See section 4.4) discovered by Sakamoto et al. (2006). At C1, the $\text{NH}_3(3,3)$ line appears in emission whereas all other inversion lines appear in absorption (Figure 6), interpreted to be due to the existence of $\text{NH}_3(3,3)$ masers, confirming the result from Ott et al. (2005). The $\text{NH}_3(3,3)$ emission for C1 is not well described by a single Gaussian and thus two Gaussians were fit to the data (Figure 9), with FWHMs of $55 \pm 3 \text{ km s}^{-1}$ and $130 \pm 10 \text{ km s}^{-1}$ and centers of $172 \pm 1 \text{ km s}^{-1}$ and $257 \pm 5 \text{ km s}^{-1}$, respectively $\text{NH}_3(3,3)\text{a}$ and $\text{NH}_3(3,3)\text{b}$.

3.2.2. H_2O masers

We identify three regions of H_2O maser emission in the data cube, labeled W1 to W3 in Figure 5 (center). The W1 water maser has been previously observed by Henkel et al. (2004) and Brunthaler et al. (2009). Spectra at these positions are shown in Figure 7. Regions W1 and W3 are seen as clear, spatially resolved peaks in Figure 5. Region W1 shows multiple velocity components with the main peak labeled W1a, and the mi-

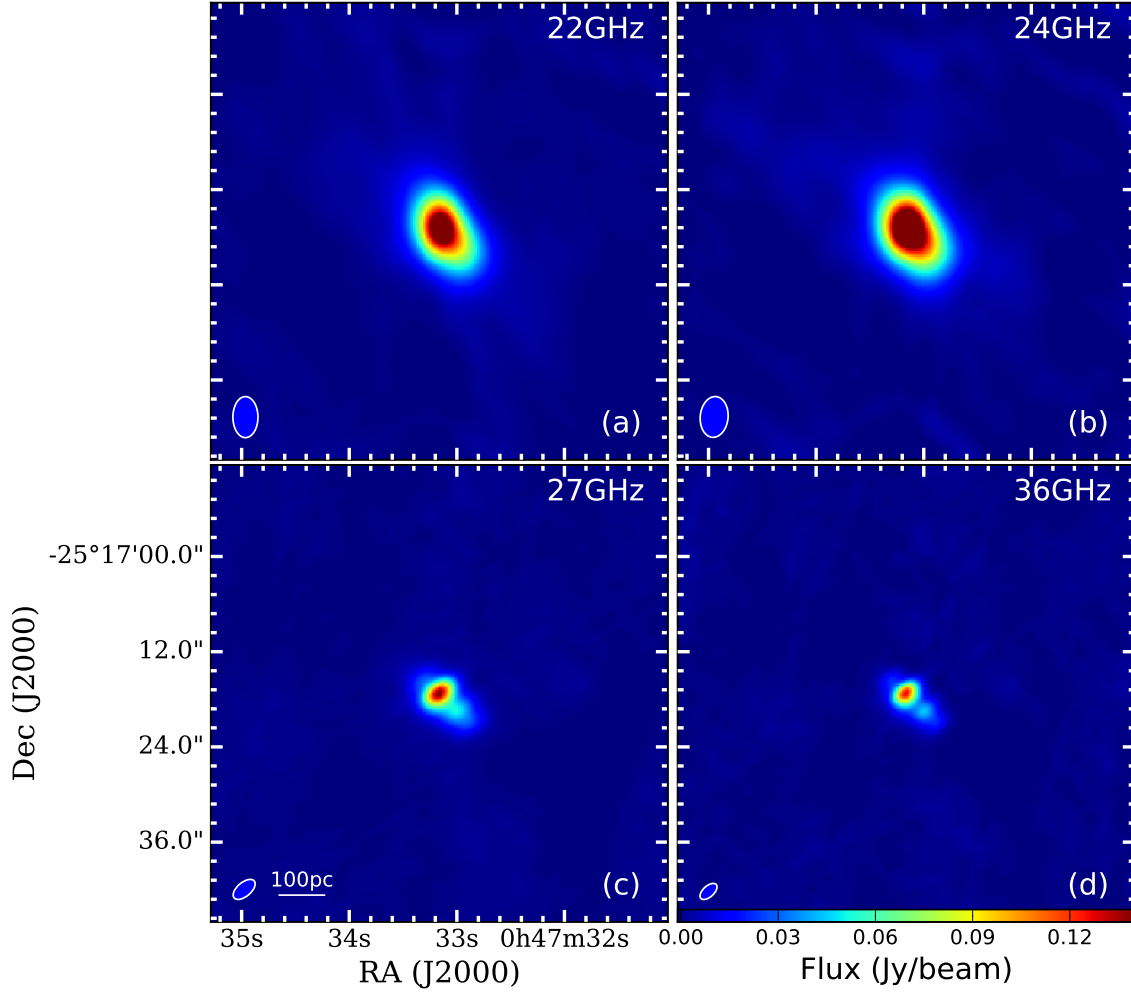


Figure 3. Images of the continuum emission from each of the 1 GHz basebands. The images are Briggs weighted and have not been smoothed to the common $6'' \times 4''$ resolution.

nor peaks labeled W1b and W1c. W2 is a faint feature which is not spatially resolved from W1 and W3, but marks the peak emission of a unique broad component shown by the shaded region in Figure 7. W2 is identified by the peak emission from the narrow feature at 273 km s^{-1} channel (Figure 7). W1 and W2 show multiple peaks in the spectrum. These were fitted with single Gaussians where appropriate. The properties are listed in Table 5. Single channel features are likely real, given our spectral resolution, but, were not fitted by Gaussians and thus their FWHMs are upper limits.

The spectrum of W2 has contributions from W1 and W3 as they are not resolved from W2. W2 is a broad pedestal spanning $\sim 100 \text{ km s}^{-1}$ centered at 233 km s^{-1} with several narrow features. The rest of its properties are listed in Table 5. This component is much better matched to systemic velocity of NGC 253. W3 is a redshifted single velocity component maser at 303 km s^{-1} .

W1a dominates region W1 and is blueshifted with respect to systemic with an observed velocity of 109 km s^{-1} . The integrated flux density of the W1a maser is

$\sim 214 \text{ K km s}^{-1}$ yielding a luminosity of $0.66 L_{\odot}$ making it a kilomaser. The extension is hard to discern in the the peak flux density and integrated flux maps (Figure 5), but it is clearly seen in the contours of the super-resolved image in Figure 10, where contours of the super-resolved image cube are plotted on the HST $\text{H}\alpha$, $\text{P}\alpha$, and the RRL $\text{H}56\alpha$ images. The super-resolved H_2O contours show the extension perpendicular to the major axis of NGC 253. This may indicate the W1 H_2O masers are related to the outflow of NGC 253 whereas W2 and W3 are spatially more consistent with the nuclear material. This result needs to be confirmed with higher resolution data. Lastly, we do not detect the $145 \text{ mJy km s}^{-1}$ H_2O maser dubbed $\text{H}_2\text{O-2}$ from Henkel et al. (2004) observed in September 2002. H_2O masers associated with YSOs and AGB stars can be variable on time scales of months (e.g. Claussen et al. 1996, Felli et al. 2007), therefore a non-detection is unsurprising.

3.2.3. 36 GHz CH_3OH masers

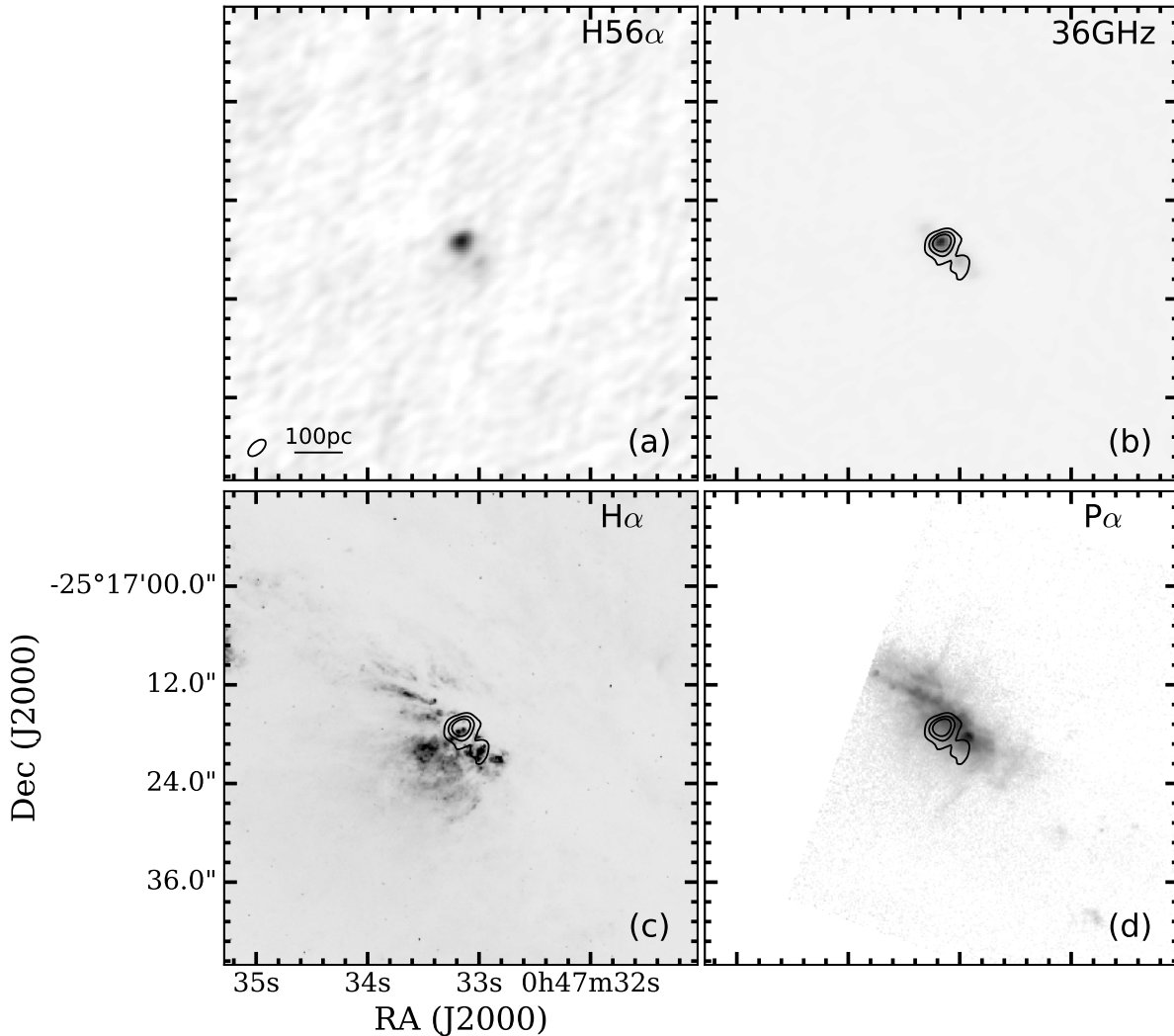


Figure 4. Comparison of star formation and outflow tracers. The contours show the 3, 6, and 9 σ contours of the naturally weighted H56 α RRL where 1σ is $0.08 \text{ Jy beam}^{-1} \text{ km s}^{-1}$. (a) H56 α RRL shows the least dust obscured star formation. (b) the 36 GHz continuum image shows a close correlation with the two knots in the RRL. (c) HST WFPC2 H α image (Watson et al. 1996). (d) HST P α (Alonso-Herrero et al. 2003) shows the outflow less well than the H α but is less obscured by dust.

Extragalactic 36 GHz CH₃OH masers were first detected by Ellingsen et al. (2014) in NGC 253 with the Australia Telescope Compact Array (ATCA)² with a $8.0'' \times 4.2''$ synthesized beam. Two sources were detected. The emission is likely not thermal in its nature, despite the large FWHM of the line, due to the total integrated intensity being ~ 20 times greater than the total integrated intensity from the Galaxy’s central molecular zone (see Ellingsen et al. 2014). We resolve the two regions previously seen in Ellingsen et al. 2014 into five different regions with masers as marked in the peak flux map. The spectra are extracted from the common reso-

lution ($6'' \times 4''$) image cubes and shown in Figure 8. The pairs M1 and M2, and M4 and M5 are not spatially resolved from each other in the common resolution cube. M1 and M2 are spectrally similar, however M4 and M5 show distinct spectral components. The CH₃OH line is very close to the edge of one of our spectral sub-bands. There are small (3.5 km s^{-1}) gaps between each sub-band where the data collected is untrustworthy, thus the channel corresponding to 160 km s^{-1} is lost. The data in this channel and the two adjacent channels are thus unreliable. We next fit single component Gaussians where appropriate. The extracted properties of the lines are shown in Table 6. The region M5 was fit with two Gaussians due to the double peak. The spectral features are narrower than the NH₃ (this paper) and ¹²CO($J = 1 \rightarrow 0$) features (Bolatto et al. 2013) from the same locations, with measured FWHMs spanning a

² The Australia Telescope Compact Array is part of the Australia Telescope, which is funded by the Commonwealth of Australia for operation as a National Facility managed by CSIRO.

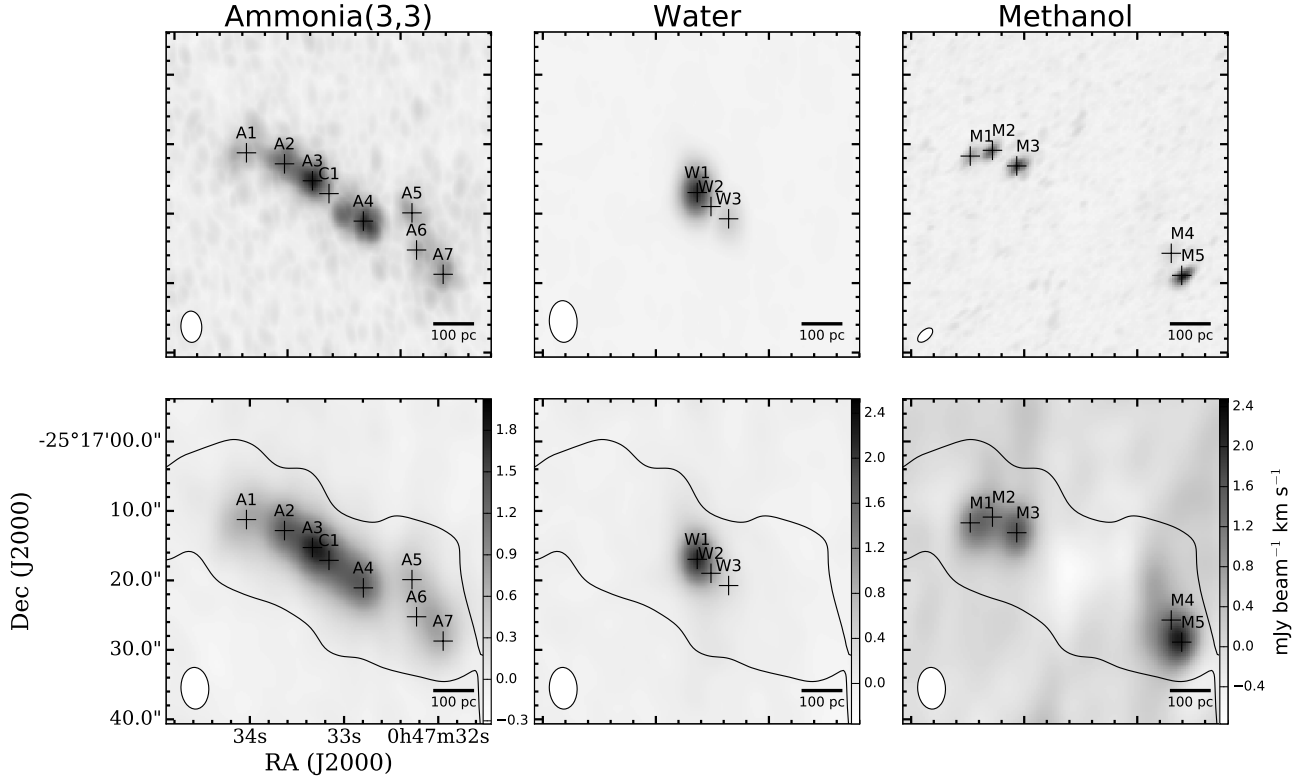


Figure 5. Images of the $\text{NH}_3(3,3)$ (left column), H_2O (center column), and CH_3OH (right column) lines. The top row shows the peak flux images of the unsmoothed naturally weighted image cubes spanning 300 km s^{-1} about systemic velocity. The bottom row shows the intensity images smoothed to the common resolution of $6'' \times 4''$. Both the peak flux and intensity images are plotted with the same greyscale. The crosses mark locations where spectra were extracted for analysis, and the continuum peak is marked C1. The contour is $60 \text{ Jy beam}^{-1} \text{ km s}^{-1}$ of $^{12}\text{CO}(J = 1 \rightarrow 0)$ from Bolatto et al. (2013) smoothed to match the resolution of the VLA data.

range of $30\text{--}80 \text{ km s}^{-1}$. The narrower widths suggest that the 36 GHz CH_3OH emission is not tracing the entirety of the molecular gas.

4. DISCUSSION

4.1. NH_3 Temperatures

One advantage of observing NH_3 is that many of its transitions are close in frequency space, and therefore can be observed with single telescope, a single observational setup, and under the same atmospheric conditions. In addition, the $< 5\%$ change in frequency between the transitions means that their respective uv coverage and the flux they resolve out are nearly identical. Rotation temperatures can then be derived from as many pairs of metastable ($J = K$) states as have been observed. Assuming optically thin conditions upper level column densities may be determined from:

$$N_u(J, K) = \frac{7.73 \times 10^{13}}{\nu} \frac{J(J+1)}{K^2} \int T_{mb} dv \quad (1)$$

where T_{mb} is the main beam brightness temperature, the column density of the upper inversion state, N_u , is in cm^{-2} , and the frequency (ν) is in GHz . A rota-

tion temperature ($T_{JJ'}$) is derived from a pair of the metastable states (J and J') by:

$$\frac{N_u(J', J')}{N_u(J, J)} = \frac{g'_{op}(2J' + 1)}{g_{op}(2J + 1)} \exp\left(\frac{-\Delta E}{T_{JJ'}}\right) \quad (2)$$

where the difference in energy between states J and J' , ΔE , is in K (the corrected version of the equation in Henkel et al. 2000 as shown in Ott et al. 2005) and the g_{op} are statistical weights depending on the NH_3 species ($g_{op} = 1$ for para- NH_3 and $J \neq 3n$ where n is an integer, and $g_{op} = 2$ for ortho- NH_3 with $J=3n$). Rotation temperatures derived from pairs of NH_3 transitions, for locations A1 to A7 are shown in Table 2. The rotation temperatures are best illustrated in the Boltzmann diagram shown in Figure 12 (top). We have plotted weighted column densities on the vertical axis and energy above the ground state on the horizontal axis. The slopes between any two points are thus proportional to the inverse rotation temperature, i.e. cold gas shows steeper slopes than warm gas (Equation 2). Notice at location C1 we see NH_3 in absorption against the continuum (Figure 6) and thus the rotation temperature must be measured differently (see next paragraph). A3

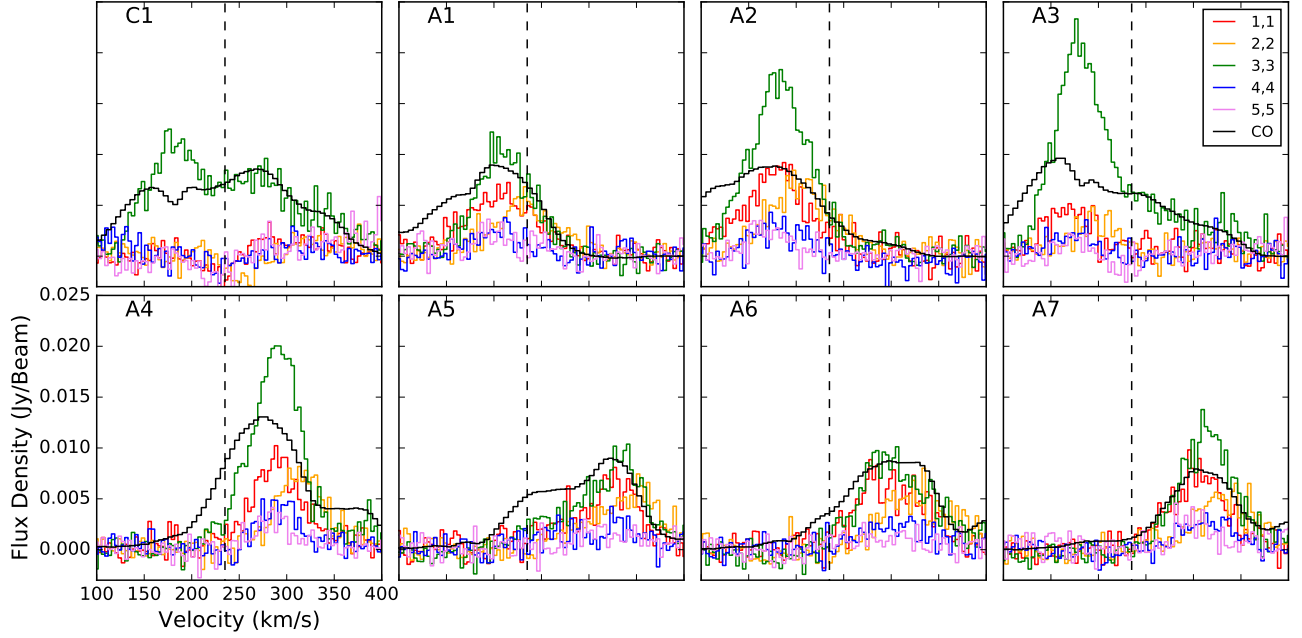


Figure 6. Spectra of the $\text{NH}_3(1,1)$ to $(5,5)$ transitions extracted from locations A1-A7 and C1. $\text{NH}_3(3,3)$, plotted in green, shows emission at all locations, whereas all the other inversion lines are absorbed toward C1. We have plotted the $^{12}\text{CO}(J = 1 \rightarrow 0)$ profile (flux density scaling factor of 0.002 and 2.5 km s^{-1} resolution) from Bolatto et al. (2013) in black for comparison. The vertical dashed line denotes the systemic velocity of NGC 253 of 234 km s^{-1} .

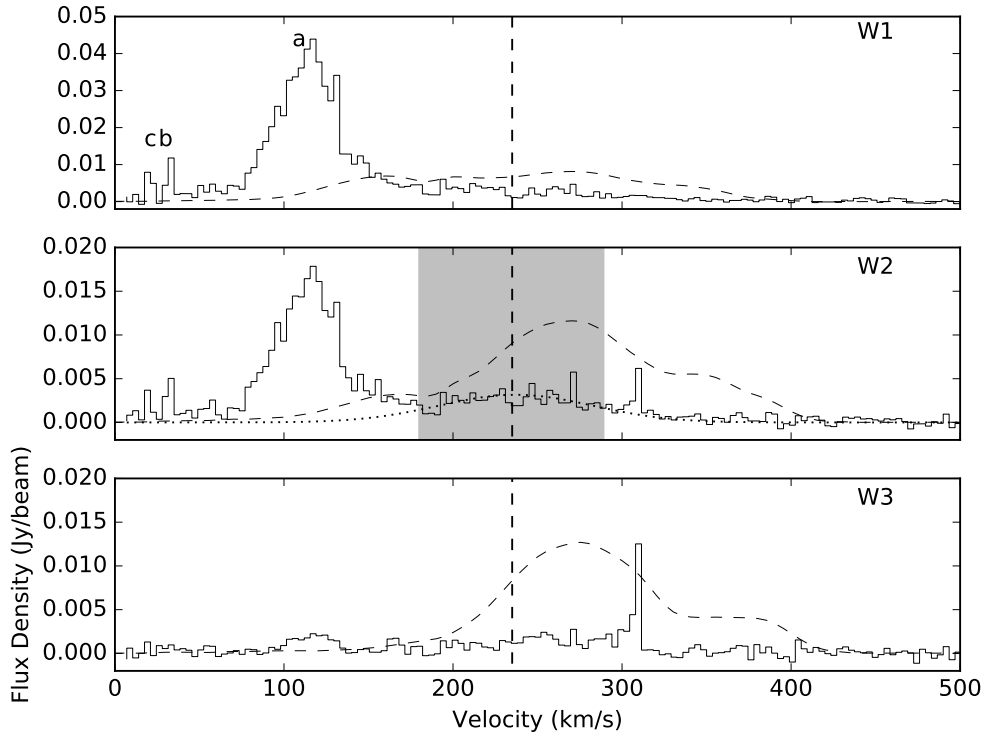


Figure 7. Water maser spectra from W1, W2, and W3. W1 shows multiple velocity components. These are labeled a to c. W2 is a spectrally broad component centered at 233 km s^{-1} . It is highlighted by the grey box and the best fit spectrum is shown by the dotted line. This component appears to consist of many individual masers. The dashed line shows the CO spectrum, with 2.5 km s^{-1} resolution, at each location scaled by 0.005 in flux density, from Bolatto et al. (2013).

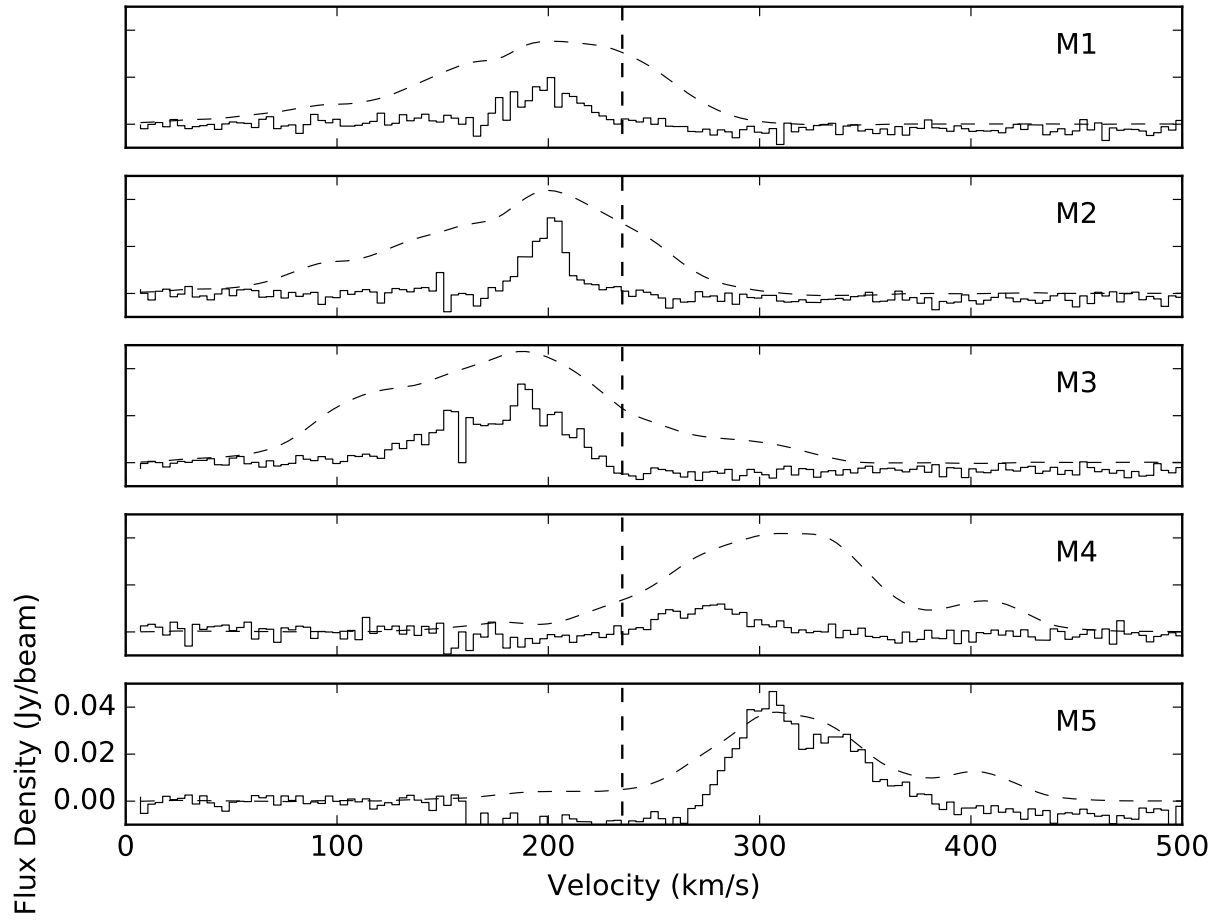


Figure 8. Methanol Spectra from M1 to M5. CO spectra are plotted with a dashed line with a flux density scaling factor of 0.01. The systemic velocity of NGC 253 is denoted with a vertical dashed line at 234 km s^{-1} .

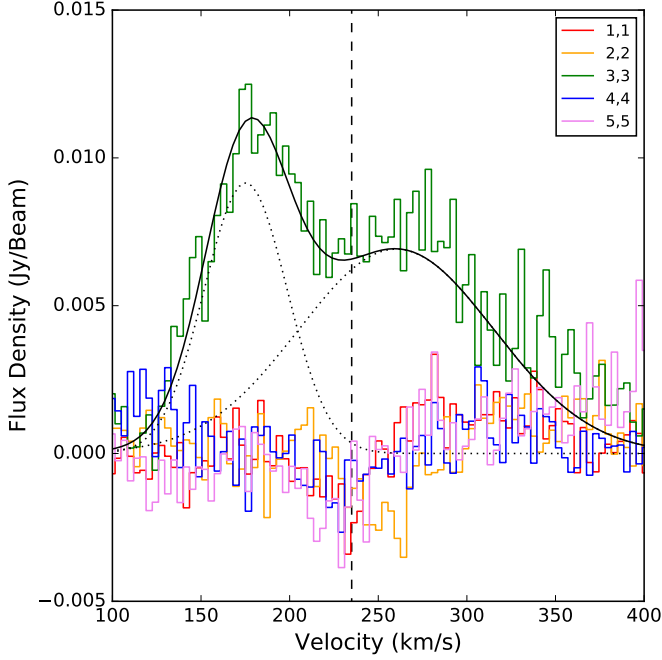


Figure 9. The NH_3 spectra towards C1. The systemic velocity of 234 km s^{-1} is shown with a vertical dashed line. All the para species of NH_3 appear in absorption while the $\text{NH}_3(3,3)$ line appears in emission. The solid black line represents the best fit two Gaussian profile. The individual Gaussian components are plotted with dotted lines.

is located ~ 0.5 beams (53 pc) from C1, thus the emission line is likely partially absorbed, making rotation temperature measurements here unreliable.

Measuring rotation temperatures from NH_3 absorption is not possible without knowing the excitation temperature T_{ex} and the optical depth τ . [Huettemeister et al. \(1995\)](#) describes the process of extracting total NH_3 column densities $N(J,K)$ (the sum of both the upper and lower inversion states):

$$\frac{N(J,K)}{T_{ex}} = 1.61 \times 10^{14} \frac{J(J+1)}{K^2 \nu} \tau \Delta\nu_{1/2} \quad (3)$$

and,

$$\tau = -\ln\left(1 - \frac{|T_L|}{T_C}\right) \quad (4)$$

where the units of $\Delta\nu_{1/2}$ (FWHM) are km s^{-1} , T_L and T_C are brightness temperatures of the line and continuum, respectively, and τ is the optical depth. We have no means to measure the transition-dependent excitation temperature, so for simplicity we assume that for each metastable transition T_{ex} is equal. In this case the rotation temperature can still be derived from Equation 2 by substituting $N(J,K)$ for $N_u(J,K)$. Rotation temperatures for C1 are shown in Table 3. Since the column density at C1 depends on the excitation temperature, the values plotted for C1 in Figure 12 are really $N(J,K)/T_{ex}$. The spatial dependence of the rotation temperature is shown in Figure 12 (bottom).

The rotational temperature is not necessarily the true thermal temperature of the gas, i.e. it is not the kinetic temperature, but rather a lower limit. We therefore employ the functions from [Ott et al. \(2011\)](#) to estimate kinetic temperatures. To convert rotation temperatures for the $\text{NH}_3(2,2)$ to $(4,4)$ ratio additional fits to the same LVG models used in [Ott et al. \(2011\)](#) from [Ott et al. \(2005\)](#) were made:

$$T_{Kin} = \begin{cases} 1.467 \times T_{24} - 6.984 & \text{for } T_{Kin} \lesssim 100 \text{ K} \\ 27.085 \times \exp(0.019 T_{24}) & \text{for } T_{Kin} \gtrsim 100 \text{ K} \end{cases} \quad (5)$$

and for the $\text{NH}_3(4,4)$ to $(5,5)$ ratio:

$$T_{Kin} = \begin{cases} 1.143 \times T_{45} - 1.611 & \text{for } T_{Kin} \lesssim 50 \text{ K} \\ 21.024 \times \exp(0.0198 T_{45}) & \text{for } T_{Kin} \gtrsim 50 \text{ K} \end{cases} \quad (6)$$

Figure 11 shows how the conversion functions fit to the LVG models. We thus derive kinetic temperatures for adjacent pairs of like species for a total of 3 measurements at each location (Table 2).

If the gas is dominated by a single kinetic temperature, all the rotation temperatures should yield that temperature. In the case that the rotation temperatures do not, either the gas must be represented by multiple kinetic temperatures, or the LVG approximation does not hold. The LVG corrected kinetic temperatures are plotted in Figure 13. The figures show remarkably little variance in the rotation and kinetic temperatures measured across all locations. We have fit a single temperature for each line pair across all locations weighted by the errors. We measure a weighted average for T_{Kin12} of $57 \pm 4 \text{ K}$, for T_{Kin24} of $134 \pm 8 \text{ K}$, and for T_{Kin45} of $117 \pm 16 \text{ K}$. The T_{Kin24} and T_{Kin45} components are consistent within the errors. The kinetic temperatures of the dense molecular gas in the central kpc of NGC 253 is therefore most consistent with a cool $\sim 57 \text{ K}$ derived from the (1,1) and (2,2) lines, and a warm $\sim 130 \text{ K}$ component derived from the weighted average of the (2,2) to (4,4) and (4,4) to (5,5) ratios.

The NH_3 transitions of NGC 253 have been of interest to many others, but most recently have been observed with the Australia Telescope Compact Array (ATCA) ([Ott et al. 2005](#)), the VLA ([Takano et al. 2005](#)), and the Green Bank Telescope (GBT) ([Mangum et al. 2013](#)). Using interferometric observations of the bar, [Ott et al. \(2005\)](#) measure rotation temperatures $T_{12} \sim 42 \text{ K}$, and [Takano et al. \(2005\)](#) measure $T_{12} \sim 26 \text{ K}$. The lower temperature measured in [Takano et al. \(2005\)](#) is likely due to a low signal to noise ratio for the $\text{NH}_3(2,2)$ line. Unlike what [Ott et al. \(2005\)](#) found, we see that a single temperature does not describe the dense molecular gas in NGC 253. [Ott et al. \(2005\)](#) observe the (1,1), (2,2),

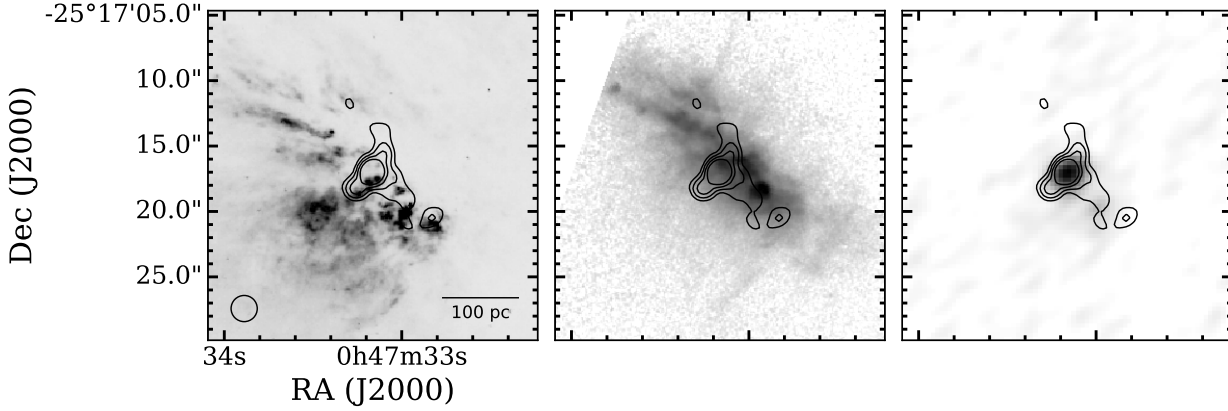


Figure 10. Super-resolved H_2O 0.02, 0.04, 0.08, and 0.16 $\text{Jy beam}^{-1} \text{ km s}^{-1}$ contours plotted on HST WFPC2 $\text{H}\alpha$ (left; [Watson et al. 1996](#)) map, HST $\text{Pa}\alpha$ (center; [Alonso-Herrero et al. 2003](#)), and RRL $\text{H}56\alpha$ (right). The synthesized beam in the bottom left corner of the left panel shows the resolution of the super-resolved cube.

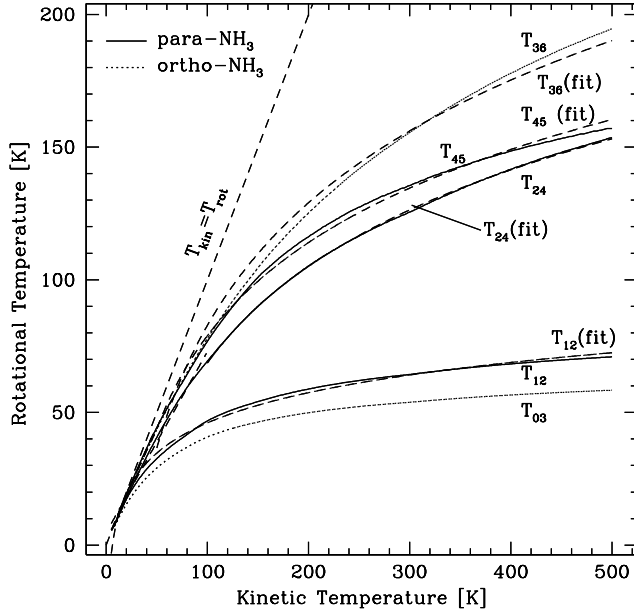


Figure 11. The solid lines represent the relationship between the kinetic temperature and the rotation temperature. The dashed lines show the fits to the models represented by equations 5 and 6, and equation 6 from [Ott et al. \(2011\)](#)

(3,3), and (6,6) lines, while our analysis, that includes the $\text{NH}_3(4,4)$ and (5,5) lines, clearly indicates a warm component not observed by [Takano et al. \(2005\)](#) and a cooler component not observed by [Ott et al. \(2005\)](#). The study by [Mangum et al. \(2013\)](#) indicates that there is a warm component to the dense molecular gas in NGC 253 as their analysis includes the $\text{NH}_3(4,4)$ line, however it is limited by the $30''$ beam of the GBT. This limits their analysis to the NW and SE velocity components, measuring T_{kin24} of 73 ± 22 K and < 150 K, respectively. It is possible that these measurements are affected by absorption in the center of NGC 253, or that they are

sensitive to a more diffuse component of the molecular gas. On average they measure a kinetic temperature of 78 ± 22 K from the $\text{NH}_3(J, K \leq 4)$ transitions for the whole galaxy, which is broadly consistent with the results presented in this paper. Modeling of the CO ladder from $J=4-3$ to $J=13-12$ from [Rosenberg et al. \(2014\)](#) yields similar results. They find evidence for three temperature and density components for the molecular ISM ranging from 60 K to 110 K and $10^{3.5} \text{ cm}^{-3}$ to $10^{5.5} \text{ cm}^{-3}$, respectively. Their observations from the *Herschel Space Observatory* have a resolution of $32.5''$. Our NH_3 analysis does not reveal any information about the density of the molecular gas. Therefore our results are only broadly consistent in terms of temperature analysis.

The spatially uniform distribution of temperatures is perhaps surprising due to the concentration of supernovae remnants in the central 500 pc ([Ulvestad & Antonucci 1997](#)). We would expect that if heating by supernovae were a dominant effect in setting the state of a GMC, then an increase in temperature towards the center of the bar would be observed as the density of supernovae increases towards the center of NGC 253. This may not be true during the bulk of a GMC's lifetime: simulations by [Murray et al. \(2010\)](#) suggest that supernovae may only contribute to heating late in the GMC's life after much of the GMC has already been disrupted by jets and radiation pressure from stars. Heating may also not be observed because supernovae might dissociate NH_3 molecules altogether in the region of greatest energy input.

4.2. LVG fitting with RADEX

To further investigate the need for multiple temperatures, we attempt to fit the data with Large Velocity Gradient (LVG) models directly. We do this to compare with the approximation to the LVG correction in section 4.1. We use RADEX ([van der Tak et al. 2007](#))

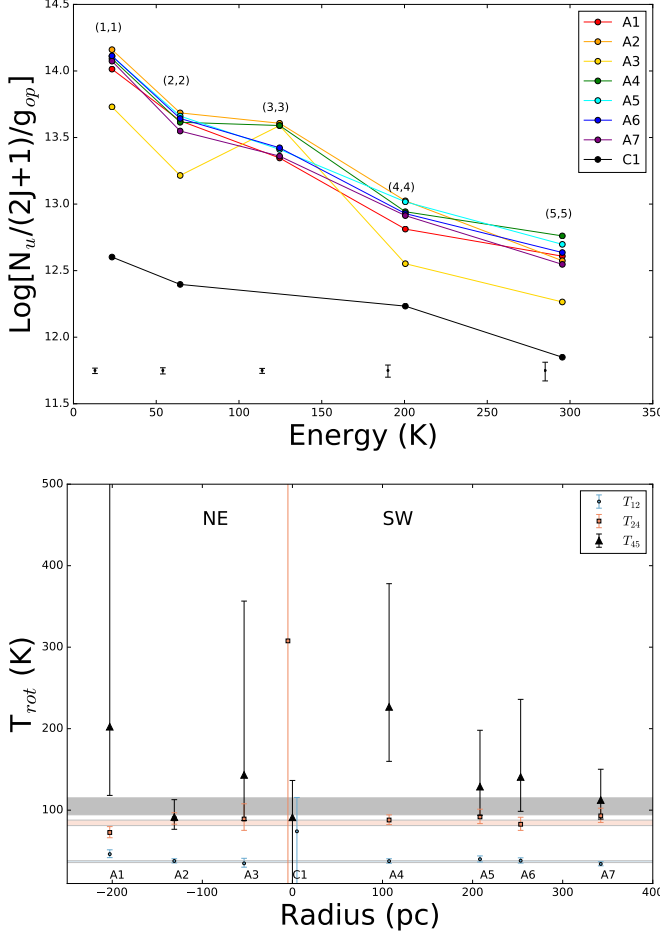


Figure 12. Top: Boltzmann diagram of the observed NH_3 transitions. The black points representing C1 are the log of the normalized N/T_{ex} not N_u , and have been scaled by a constant 0.85 preserving the proportionality of T_{rot} . Error bars are plotted along the bottom and are the unweighted average of the individual metastable states from each location. Bottom: rotation temperatures derived from metastable line pairs. Error bars are measured from the minimum and maximum column densities of an individual line. The horizontal bars represent single temperature fits to the data. The height of the bar represents the uncertainty.

with collisional coefficients from the LAMBDA database (Schöier et al. 2005). RADEX was not used by Ott et al. (2005) and Ott et al. (2011), however it does make use of some of the same collisional coefficients. The collisional coefficients from the LAMBDA database cover temperatures up to 300K, thus the kinetic temperature axis of the grid spans 0-300 K in steps of 3 K. The collider (H_2) volume density and NH_3 column density axes of the grid are logarithmically sampled respectively from 10^2 - 10^6 cm^{-3} , and from 10^{13} and 10^{17} cm^{-2} with 100 steps each. In the LVG approximation the ratio $N/\Delta v$ is the independent variable, however in RADEX the column density and line width are specified separately. We specify a line width calculated from the weighted mean of 74 km s^{-1} from all the para species of NH_3 in Table

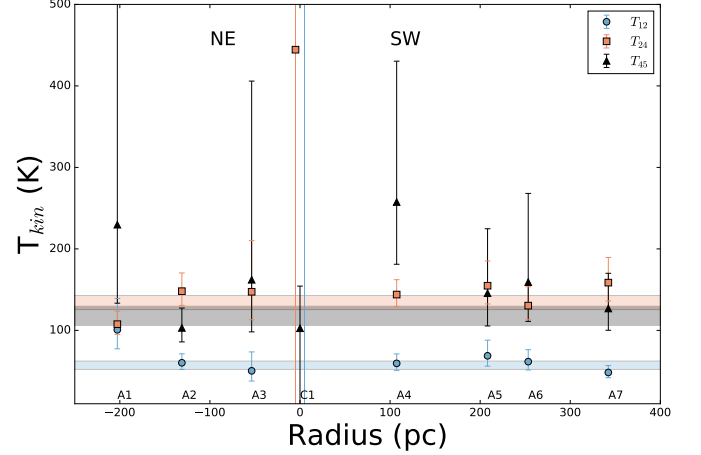


Figure 13. Estimated kinetic temperatures after applying the LVG correction from Ott et al. (2005). The horizontal bars represent single temperature fits to individual line pairs with the height representing the uncertainty. We see the need for a two temperature description of the molecular ISM. The derived temperatures from the J,K= 2,4,& 4,5 ratios are consistent with a $\sim 130 \text{ K}$ temperature component and the J,K=1,2 ratio measures a $\sim 57 \text{ K}$ component.

2.

The fits were carried out for each ratio of adjacent $J=K$ para- NH_3 species. The results are tabulated in Table 7 and qualitatively displayed in Figure 14. In the figure the median fitted temperature is drawn with a dashed line between the 1σ confidence contours. The errors are calculated from the rms of the median fit for values above a critical density of $\sim 10^3$ Cheung et al. (1968). Below this density there is a slight upturn to the temperature parameter suggesting that high-T and low-n may excite ammonia at relatively low densities. This high-T low-n condition is unlikely as many higher critical density gas tracers have been observed with similar structure in the nucleus of NGC 253 Meier et al. (2015). The H_2 density is not well constrained, with error bars that span the entirety of the sampled parameter space, consistent with NH_3 not being a density probe. Generally, the fits are well behaved with the exception of the (4,4) to (5,5) ratio (not shown), for which the best fit solutions are poorly constrained and tend towards the edge of the temperature axis with values of $\sim 300 \text{ K}$. It is possible that there is a component that is hotter than our temperature range allows, but we cannot provide any meaningful estimates from the fitting. In contrast to the (4,4) to (5,5) ratio, the (1,1) to (2,2) and (2,2) to (4,4) ratios are well behaved. The solutions cover two regions of parameter space indicating a warm and cool component (Table 7). The spatial distribution of temperatures is mostly uniform for the cool component, derived from line ratios $\text{NH}_3(1,1)/\text{NH}_3(2,2)$, with an average temperature of $74 \pm 12 \text{ K}$, and likewise for the warm component, derived from the $\text{NH}_3(2,2)/\text{NH}_3(4,4)$

ratio, with an average temperature of 145 ± 14 K. This is broadly consistent with the analysis in §4.1.

4.3. Nature of the 36 GHz CH₃OH masers

The nature of the 36 GHz methanol masers appears different from what we understand of their Galactic counterparts. Yusef-Zadeh et al. (2013) performed a CH₃OH maser survey of the inner 160 x 43 pc of the Galaxy. We will use their study as a template to address CH₃OH emission in NGC 253. The CH₃OH line widths in NGC 253 span tens of km s^{-1} whereas individual Galactic CH₃OH masers tend to span a few km s^{-1} . The NGC 253 36 GHz line is spectrally resolved and multiple components can be fitted (see Table 6). The maser with the largest flux found by Yusef-Zadeh et al. (2013) (number 164) is $\sim 470 \text{ Jy km s}^{-1}$, which corresponds to an isotropic luminosity, assuming a distance of 8 kpc, of $1.1 \times 10^{-3} L_{\odot}$. By comparison the most luminous CH₃OH maser in NGC 253 is $1.63 L_{\odot}$. This would mean that the beam averaged class I CH₃OH masers in NGC 253 are about a thousand times more luminous than the most luminous CH₃OH maser found by Yusef-Zadeh et al. (2013). Alternatively, there may be thousands of bright masers at similar velocities in one $6'' \times 4''$ beam. Surveys of Class I methanol masers in supernovae remnants (e.g. McEwen et al. 2014 & McEwen et al. 2016) have revealed spectrally similar results to Yusef-Zadeh et al. (2013) with narrow spectral features spanning a few km s^{-1} . At our spatial resolution of 101×67 pc the CH₃OH emission is not well resolved, and the entirety of the Yusef-Zadeh et al. (2013) survey corresponds approximately to the size of one of our beams. Since there are > 300 sources in a similar region of the Galaxy, and the NGC 253 spectra show multiple velocity components, it is possible that there are many components at each location. The broad spectral profile could be constructed from many masers from protostellar outflows or supernovae remnants.

4.4. Impact of Superbubbles on the Dense Molecular ISM

Sakamoto et al. (2006) find two superbubbles in NGC 253 in $^{12}\text{CO}(J = 2 \rightarrow 1)$ emission. The shells are ~ 100 pc in diameter, have masses of order $10^6 M_{\odot}$ and kinetic energies of order 10^{46} J, suggesting winds and supernovae from a super star cluster, or a hypernova, as the creation mechanism. Close to the location where these superbubbles interact with dense molecular gas, as traced by NH₃, we observe CH₃OH masers. Figure 15 shows $^{12}\text{CO}(J = 1 \rightarrow 0)$ channel maps of the superbubbles with CH₃OH contours overlaid. There are two groups of masers. The first is on the northeast side of the galaxy and consists of M1, M2 and M3. The other group consists of M4 and M5 on the southwest

side (Figure 5). All the CH₃OH masers except M3 can be associated with the Sakamoto superbubbles. The association indicates that these masers exist where clouds are influenced by the expanding superbubbles. This relationship is also indicated by larger NH₃ linewidths at the locations A1, A5, and A6, which are nearest the masers and the superbubbles.

The larger observed linewidths are not likely a result of more turbulence within the clouds. A comparison with the GMCs from Leroy et al. (2015) suggests that the broader observed line widths in our data are likely a result of beam smearing effects. With a $2''$ beam Leroy et al. (2015) are able to resolve individual clouds. Their clouds are clearly dominated by turbulence, as in all cases the thermal linewidth is $< 1 \text{ km s}^{-1}$ as calculated from our NH₃ derived temperatures. Using an average temperature of 117 K derived from our NH₃ analysis, the mean thermal energy stored in the Leroy et al. (2015) clouds is $\sim 5 \times 10^{43}$ J, whereas the mechanical energy stored, as derived from turbulent linewidths, is $\sim 1 \times 10^{46}$ J. The turbulent linewidths of individual GMCs detected in Leroy et al. (2015) appear unaffected by the impact of the expanding superbubbles, and in fact appear uniform across the entire central molecular bar (Figure 17). The larger NH₃ linewidths observed with a larger beam suggest instead that the superbubbles are imparting mechanical energy resulting in bulk translational motion of the GMCs.

The relationship of the clouds to the masers is shown by Figure 16, which plots kinetic temperatures T_{kin12} and T_{kin24} derived from NH₃ against the mean FWHM of the NH₃ transitions. The figure shows little temperature variation toward the shocks traced by CH₃OH. If there is shock heating of the dense molecular gas it must be highly localized to areas much smaller than the beam such that it does not affect the overall kinetic temperature measured with ~ 100 pc spatial resolution.

4.5. The Outflow, Masers, and Starburst

4.5.1. NH₃(3,3) masers

The location of the continuum peak (C1) is also the locus of the starburst and the central base of the molecular and ionized bipolar outflow. Here the para-NH₃ lines are not observed in emission, however the ortho-NH₃(3,3) line is. We did not detect any other ortho species of NH₃ at this location to compare with, however Ott et al. (2005) did observe the ortho (6,6) species to be in absorption at our location C1. Since NH₃(3,3) is the only ortho-NH₃ species observed in emission at this location, we corroborate the interpretation from Ott et al. (2005) that the NH₃(3,3) line is masing here. The spectral line (Figure 6) could not be fit with a single Gaussian, but rather two Gaussians centered at 172 km s^{-1} and 257 km s^{-1} with widths of 55 km s^{-1} and

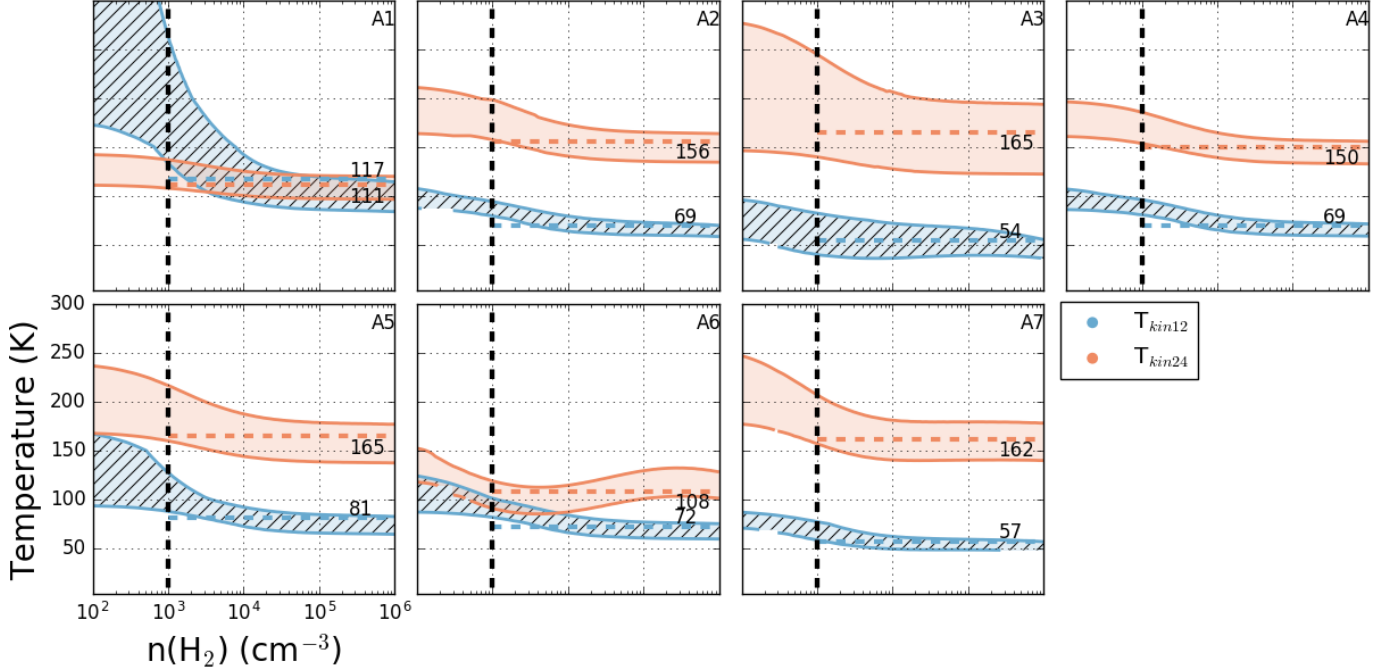


Figure 14. Best fits of the LVG models to the data. The blue hatched region represents the NH_3 J=1,2 ratio, and the red region NH_3 J=2,4. The shaded areas represent the 1σ errors in the fit. The horizontal dashed line represents the the median temperature fit for densities exceeding the critical density of NH_3 of 10^3 (vertical line)

130 km s^{-1} , respectively $\text{NH}_3(3,3)\text{a}$ and $\text{NH}_3(3,3)\text{b}$ (see Figure 9). The existence of the $\text{NH}_3(3,3)$ maser suggests that the collision rate in the center of NGC 253 increases or there exists an excess of infrared photons in the center in order to pump this maser. Currently, there is one other known extragalactic source of $\text{NH}_3(3,3)$ masers apart from NGC 253: the Seyfert galaxy NGC 3079 (Miyamoto et al. 2015). Both galaxies host outflows, but NGC 3079 is host to an active galactic nucleus (AGN). It hosts a star formation rate of $2.6 \text{ M}_\odot \text{ yr}^{-1}$ over 4 kpc (Yamagishi et al. 2010) measured from 1-1000 μm emission. Attribution to an AGN driven wind might be favored because the starburst is weak. Since the mechanism driving the outflows in these galaxies is different, we hypothesize that in both cases it is the collision of the hot ionized outflow cone with the surrounding material that results in the $\text{NH}_3(3,3)$ masers.

4.5.2. H_2O masers

The H_2O masers are located within the centermost 200 pc. Being at the center of the starburst it is likely that all these masers are star formation related. Brunthaler et al. (2009) investigated this location with the VLBA and inferred a pure starburst nature of the masers due to their similarity to Galactic H_2O masers and spatial coincidence with supernovae remnants. Our data, while much lower in resolution, indicate that W1 may be extended perpendicular to the disk and aligned with the bipolar ionized gas outflow (Figure 10). The spectrum

shows evidence of multiple components (Figure 7). W2 contains many individual components within a velocity space $\sim 100 \text{ km s}^{-1}$ wide centered at systemic velocity and includes contributions from W1 and W3. W3 is a single component maser located to the southwest of the nucleus.

W3 is the simplest H_2O maser to explain. It is cospatial with an H II region seen in Figure 4 and has a narrow spectrum. It is likely associated with a massive star or stars in that region. Its isotropic luminosity of $2 \times 10^{-2} L_\odot$ is consistent with luminosities of AGB and YSO H_2O masers in the Galaxy (e.g Palagi et al. 1993).

The H_2O maser W1 is the clear oddity in NGC 253. W1 is most clearly seen in the super-resolved image Figure 10. There are three components with observed velocities in the range 25-109 km s^{-1} , while the systemic velocity of the galaxy is 234 km s^{-1} . The W1 maser emission does not follow the kinematics of the dense molecular ISM (Figure 7). The most luminous and broad component is centered at 109 km s^{-1} . According to Brunthaler et al. (2009) this maser emission is associated with supernova remnant TH4 (Turner & Ho 1985 and Ulvestad & Antonucci 1997). However, because of the extreme conditions under which H_2O is known to mase, in addition to the locations and velocities, and because no H_2O masers are found in Milky Way supernova remnants (Claussen et al. 1999 and Caswell et al. 2011), we hypothesize that these masers are tracing shocks in entrained material in the outflow.

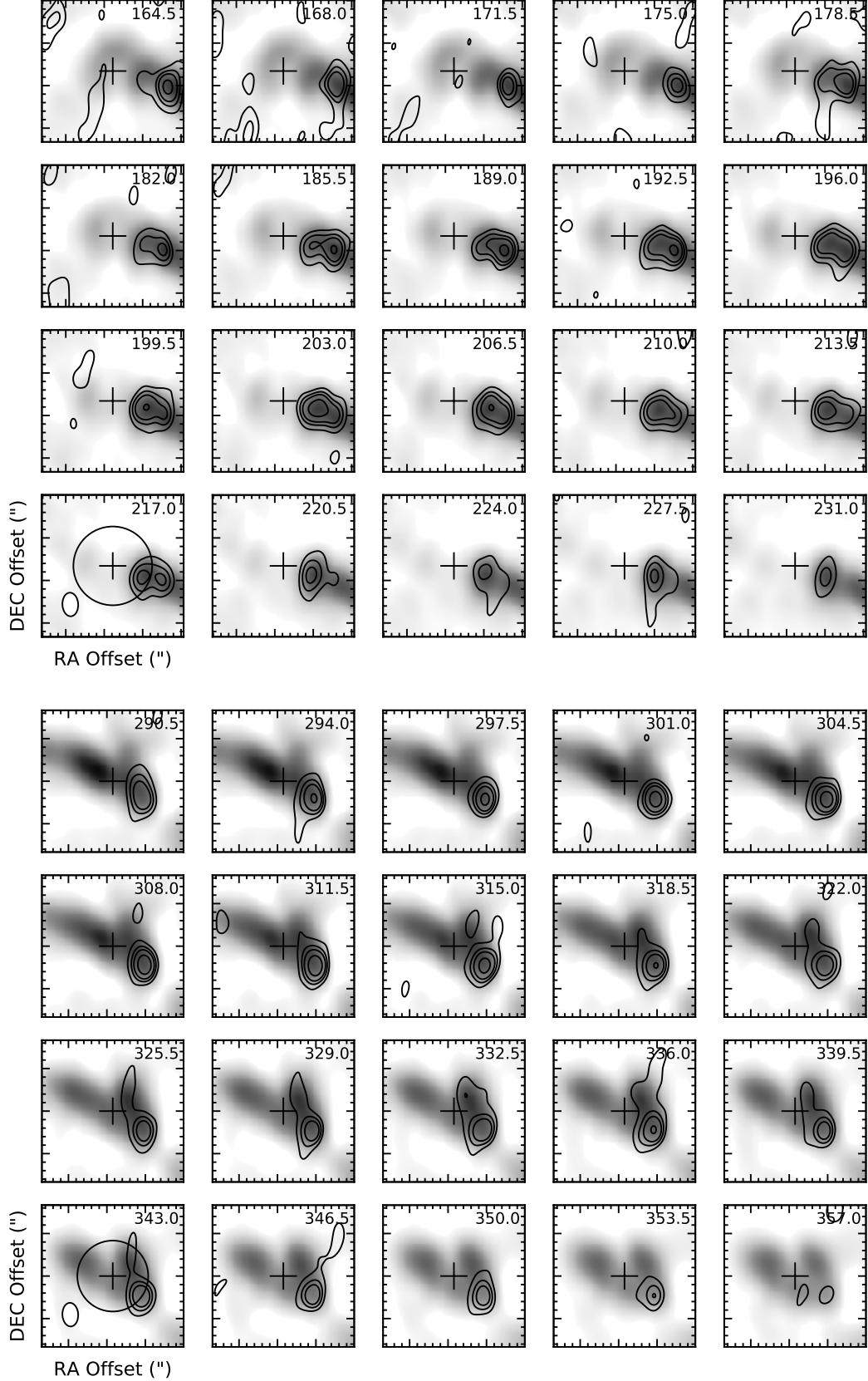


Figure 15. Channel maps of the regions containing the superbubbles found by Sakamoto et al. (2006). The top block shows the eastern superbubble (RA: $00^{\text{h}}47^{\text{m}}34.64^{\text{s}}$, DEC: $-25^{\circ}17'09.5''$) and the bottom block shows the western superbubble (RA: $00^{\text{h}}47^{\text{m}}32.53^{\text{s}}$, DEC: $-25^{\circ}17'24.0''$). Each box is $18'' \times 18''$. The black circle shows the diameter of the superbubbles measured by Sakamoto et al. (2006). The gray scale image shown is $^{12}\text{CO}(J=1 \rightarrow 0)$ emission from Bolatto et al. (2013). The 1, 2, 3, and 5 times $4.5 \text{ mJy beam}^{-1}$ contours of CH_3OH are shown and the velocity in km s^{-1} is shown in the top right of each panel.

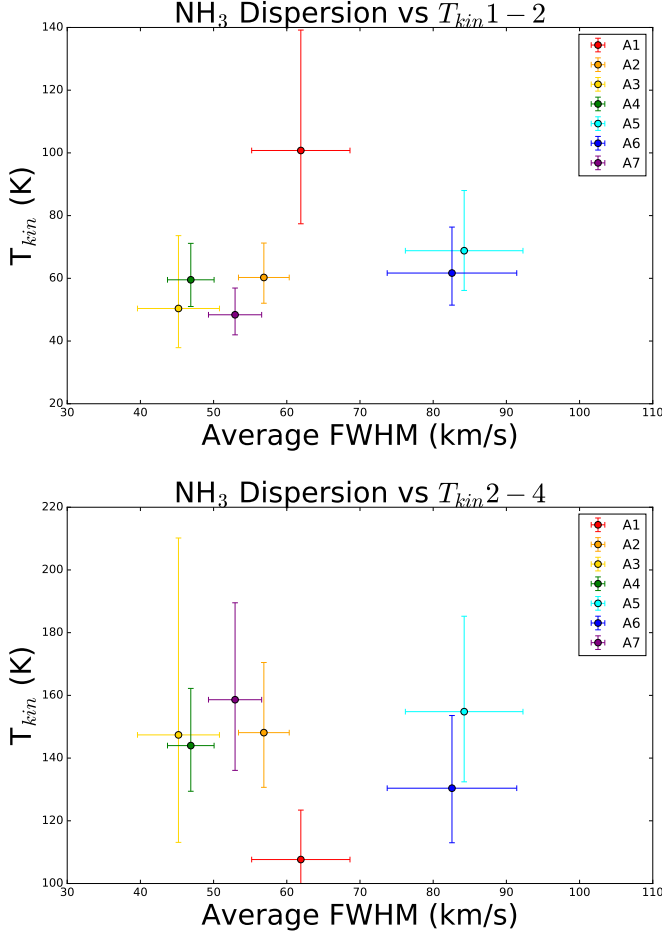


Figure 16. Plots of the average FWHM vs. derived kinetic temperatures from pairs of the NH_3 $J=1,2$ (top) and $J=2,4$ (bottom) lines.

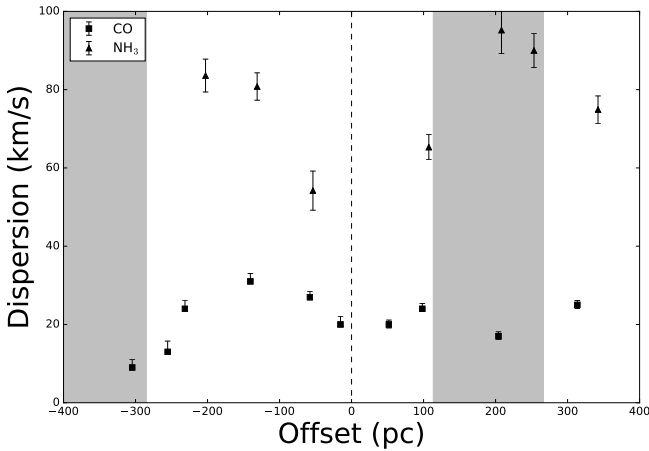


Figure 17. The measured FWHM as a function of offset from the continuum peak C1. The circles represent the FWHM of $^{12}\text{CO}(J=1 \rightarrow 0)$ from Leroy et al. (2015) and the triangles represent the $\text{NH}_3(1,1)$ FWHM. The areas of the expanding superbubbles are shaded grey.

We consider three possibilities for the origin of the masers. First, Figure 11 in Strickland et al. (2002) show possible anatomies of starburst driven outflows in NGC 253. In this picture the W1 H_2O masers likely trace dense gas clumps closest to the starburst center or shocked dense gas entrained in the outflow. The observed velocities are consistent with the Strickland model predictions for outflow velocities of order 100 km s^{-1} . A model of a conical outflow developed by analyzing optical integral field unit data in Westmoquette et al. (2011) presents a more direct view of the outflow in NGC 253. Their data show that the ionized gas associated with the base of the outflow is blueshifted $\sim 100 \pm 50 \text{ km s}^{-1}$ with respect to systemic. This is a good match to the observed velocities of W1a to W1c suggesting that there are shocks related to the outflow. The origin of the shocks remains unknown as we do not see a spatial separation of W1a, b and c, even in the super-resolved image cube. We hypothesize that they may be shocks in entrained material in the outflow, or collisions with dense gas that funnels the outflow out of the galactic plane. In this picture W2 does not have observed velocities that match either the Strickland et al. (2002) or Westmoquette et al. (2011) models of the outflow. The velocity center of W2 matches the systemic velocity of NGC 253, suggesting that it may exist in a molecular torus about the center. The velocities of the $\text{NH}_3(3,3)$ masers and the $^{12}\text{CO}(J=1 \rightarrow 0)$ spectrum from the same location are similar (Figure 7). In the Strickland models the $\text{NH}_3(3,3)$ and W2 H_2O masers would exist where the outflow impacts the unperturbed disk triggering star formation. The W2 H_2O narrow components are likely generated by YSOs in the nuclear starburst, and the NH_3 masers are likely star forming sites like that of DR 21 (Wilson & Mauersberger 1990) or W51 (Goddi et al. 2015) in the Galaxy.

The second possibility is that, while the W1 masers still originate in the outflow, the W2 masers do not trace a molecular torus, but rather their velocity extent is due to a two-sided outflow. Here the portion of W2 redshifted with respect to systemic is tracing the receding side of the outflow. However, the receding side is not as well understood because it is obscured by dust and tipped away from the observer, making optical and soft X-ray observations difficult. Westmoquette et al. (2011) find it impossible to model the receding outflow cone, and the analysis from Strickland et al. (2002) is focused on kpc scales. Therefore current evidence for the receding outflow is limited to hundreds of pc displacement from the disk. As H_2O masers are unaffected by dust obscuration, this picture implies fewer shocked regions as traced by H_2O on the receding side of the outflow, or that other masers in the receding outflow are unobserved due to line of sight effects. In this case the W1

masers would exist as in the first picture.

Lastly, it is possible that the W1 H₂O masers are not related to the outflow at all, leaving us with the difficulty of explaining their velocities. Brunthaler et al. (2009) noticed that W1 is cospatial with the supernova remnant TH4. The W2 masers in this case would likely be gas in the molecular torus as in the first picture or associated with known supernova remnants at their location. With an rms of 12 mJy it is unlikely that Brunthaler et al. (2009) would have seen the fainter masers comprising W2. Our spatial resolution makes this problem difficult to solve, thus deeper high-resolution observations are necessary.

4.6. Millimeter Molecular Lines

In order to reveal the underlying properties responsible for the observed temperatures and masers, we compare with images of several molecular species from Meier et al. (2015) who observed NGC 253 with ALMA in the millimeter range. We have chosen five molecules that trace PDRs (113.40 GHz CN(1-0;1/2-1/2); Rodriguez-Franco et al. 1998), intermediate densities (89.18 GHz HCO⁺ (1-0)) found in both diffuse and dense clouds (Turner 1995), gas densities greater than $3 \times 10^4 \text{ cm}^{-3}$ (88.63 GHz HCN (1-0) Gao & Solomon 2004), weak shocks (89.92 GHz HNCO (4_{0,4} – 3_{0,3} Meier & Turner 2005), and strong shocks (86.84 GHz SiO (2-1; $\nu = 0$) García-Burillo et al. 2000). The largest spatial scale of in the sampled by Meier et al. (2015) is $18''$. They compare the ALMA interferometric maps with single dish observations and find that 50%-100% of the total flux is recovered. The largest spatial scale of the VLA D configuration at K band of $66''$ thus we expect less flux to be resolved out by the VLA than for ALMA. The maximum uncertainty of the VLA to ALMA line ratios could consequently be increased by a factor of two. The resolution of the ALMA cubes is $\sim 2'' \times 2''$. The HCN map, with NH₃(3,3) contours in white, is shown in Figure 18. Both molecular morphologies are well correlated. This suggests that these molecules are tracing similar environments. We show the PDR and dense gas tracers, CN and HCO⁺, with NH₃(3,3) contours overlaid (Figure 19 top). Like HCN, CN and HCO⁺ trace similar regions as NH₃.

For the shock tracers, HNCO and SiO, we have overplotted the naturally-weighted unsmoothed 36 GHz CH₃OH contours (Figure 19 bottom). The CH₃OH masers are well correlated with HNCO and SiO at the sites of the Sakamoto et al. (2006) superbubbles, however the centermost 200pc remains bright in SiO whereas HNCO dims (Meier et al. 2015). The CH₃OH masers appear much better correlated with HNCO than SiO. We take the dominant source of error in the individual molecular maps to be the 10% estimate in the absolute

flux density calibration. To estimate relative intensities the individual ALMA maps were smoothed to the common resolution of $6'' \times 4''$ to match our VLA data. We then normalized these maps by the HCN map. Line ratios were then measured at locations A1-A7 and C1. The line ratios are shown in Figure 20 plotted in black with the $T_{\text{Kin}12}$ shown in red and $T_{\text{Kin}24}$ shown in blue.

The cold and warm temperature components of the molecular gas do not correlate well with PDR tracers (CN), intermediate densities (HCO⁺), weak shocks (HNCO), or strong shocks (SiO). We interpret the plots in Figure 20 to mean that none of the selected processes relate to the heating and cooling of the dense molecular ISM on 100 pc scales in NGC 253. This possibly means that cosmic rays are the dominant source of heating in the center of NGC253, or that the dominant heating source destroys NH₃ molecules and we are only sensitive to less impacted molecular gas.

At the same time, we measure a relative decrement of HNCO in the center compared to the locations with 36 GHz CH₃OH masers and the expanding Sakamoto et al. (2011) superbubbles. In the case of NGC 253 Meier et al. (2015) argue that the relative decrement of HNCO is a consequence of dissociation in the PDR dominated center. The lack of methanol masers on the eastern side of the west superbubble is consistent with dissociation closer to the center. It is interesting that the non-thermal 36 GHz CH₃OH correlates with the HNCO. A similar tight correlation has been observed between HNCO and thermal CH₃OH in nuclei (e.g. Meier & Turner 2005, Meier & Turner 2012). This is further evidence that the 36 GHz CH₃OH is tracing similar shocked regions. SiO is also enhanced near the superbubbles. However SiO is more uniformly distributed in the center 300 pc of NGC 253 where we did not observe any 36 GHz CH₃OH masers suggesting that the 36 GHz CH₃OH maser is more closely related to weak shocks than strong shocks. Position velocity (PV) cuts were made through the eastern and western groups of masers. Figure 21 shows the PV cuts through the HCN cube with the naturally weighted 36 GHz methanol contours in black. The HCN cube reveals a few shell-like structures. The methanol masers are well correlated with the edges of the shells strengthening the connection between the shocks and the dense molecular gas.

5. SUMMARY

We have provided analysis of VLA observations of the dense gas and masers associated with the nuclear starburst in NGC 253. We conclude the following:

1. We have detected NH₃(1,1), (2,2), (3,3), (4,4), and (5,5) in the central kpc of NGC 253. NH₃(9,9) is detected in only one location. No NH₃ is observed

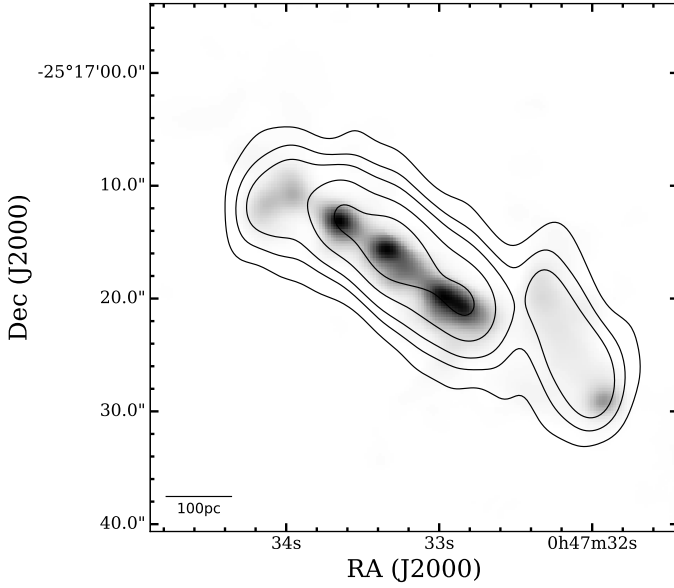


Figure 18. HCN map from [Meier et al. \(2015\)](#) in greyscale with $\text{NH}_3(3,3)$ 3, 6, 9, 15, and $24 \times 4.8 \text{ K km s}^{-1}$ contours.

in the molecular outflow.

2. We find the molecular gas in NGC 253 to be best described by a spatially uniform two kinetic temperature model with a warm 130 K component and a cool 57 K component. The continuum peak (C1) may indeed be hotter as it is closer to the starburst, but absorption of the metastable para- NH_3 lines make temperature measurements less accurate. Direct LVG analysis corroborates a two temperature model of NGC 253, though with a cool component of 74 K and a warm component of 145K. The LVG analysis does hint at a hotter component greater than 300 K as traced by the $\text{NH}_3(4,4)$ and $\text{NH}_3(5,5)$ ratio. The temperature distribution is not well correlated with PDRs, weak shocks, or strong shocks, and is constant over the central kpc.
3. We confirm the result from [Ott et al. \(2005\)](#) suggesting that there exist $\text{NH}_3(3,3)$ masers in the nucleus of NGC 253. There is currently only one other known source of extragalactic $\text{NH}_3(3,3)$ masers, NGC 3079 ([Miyamoto et al. 2015](#)). Both galaxies host outflows, but in NGC 253 the outflow is driven by a starburst whereas in NGC 3079 it is likely driven by an AGN.
4. Expanding superbubbles do not appear to heat the gas in NGC 253. A comparison with the results from [Leroy et al. \(2015\)](#) shows that the

linewidths are dominated by turbulent motions within a GMC. The large NH_3 linewidths are likely due to the bulk motion of the GMCs.

5. Three H_2O maser features have been observed. The H_2O maser W1 is coincident with the continuum peak. We show indications emission is extended along the minor axis of the galaxy, the spectrum suggests multiple components and the velocities are more similar to the outflow than the disk. It is likely that this maser is related to the bipolar outflow of ionized gas, though other explanations are possible. High resolution followup observations are needed to confirm a relationship with the bipolar outflow.

W2 is located to the southwest of W1 and shows multiple spectrally unresolved masers with velocities centered about systemic, suggesting these masers exist in a circumnuclear torus. It is also possible that W2 may in part trace the receding side of the outflow. W3 is unresolved and located to the southwest of W1 and W2. Its progenitor is likely a massive star.

6. We detect five regions with 36 GHz CH_3OH masers at the outside edge of the central kpc as traced by NH_3 . The spatial proximity and velocities suggest a relationship with known superbubbles. Position velocity cuts show that all the 36 GHz methanol masers may be related to shell-like features. The 36 GHz CH_3OH morphology and HNC are similar. This similarity suggests that both HNC and 36 GHz methanol masers are tracing similar conditions.

Our analysis reveals the properties of the dense molecular ISM in along the central kpc of NGC 253 using centimeter and millimeter emission and absorption lines. We have uncovered relationships with the bipolar outflow, expanding molecular bubbles, and the nuclear starburst.

Mark Gorski acknowledges support from the National Radio Astronomy Observatory in the form of a graduate student internship, and a Reber Fellowship. We would like to thank Alberto Bolatto and Adam Leroy for sharing the ALMA image cubes. This research has made use of the NASA/IPAC Extragalactic Database (NED), which is maintained by the Jet Propulsion Laboratory, Caltech, under contract with the National Aeronautics and Space Administration (NASA) and NASA's Astrophysical Data System Abstract Service (ADS).

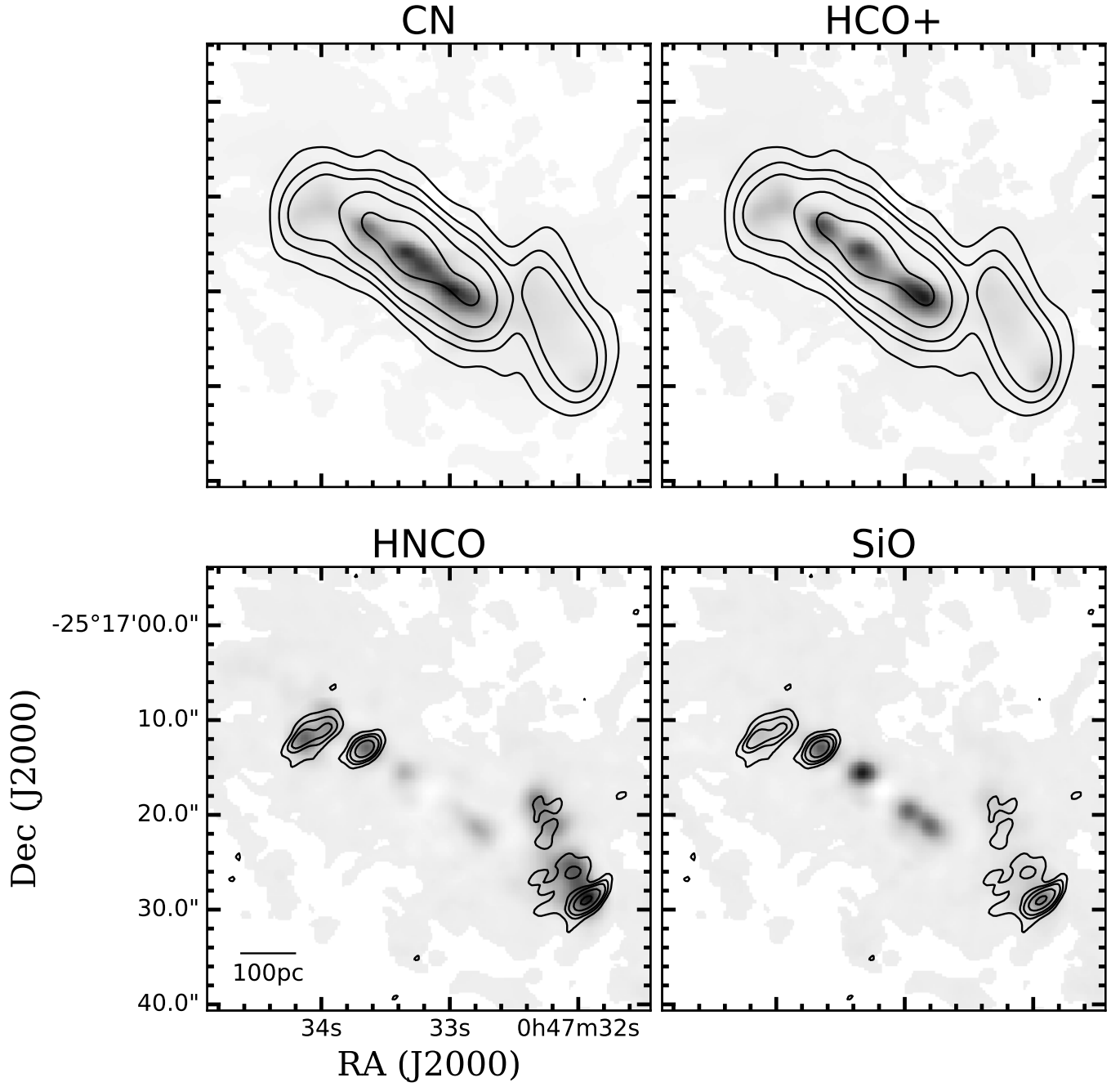


Figure 19. The top row shows the PDR tracer CN(left) and intermediate density tracer HCO⁺(right) (Meier et al. 2015) with 3, 6, 9 15, and 24 σ contours of NH₃. The bottom row shows shock tracers HNCO and SiO (Meier et al. 2015) with 3, 6, 9 15, and 24 σ contours of CH₃OH.

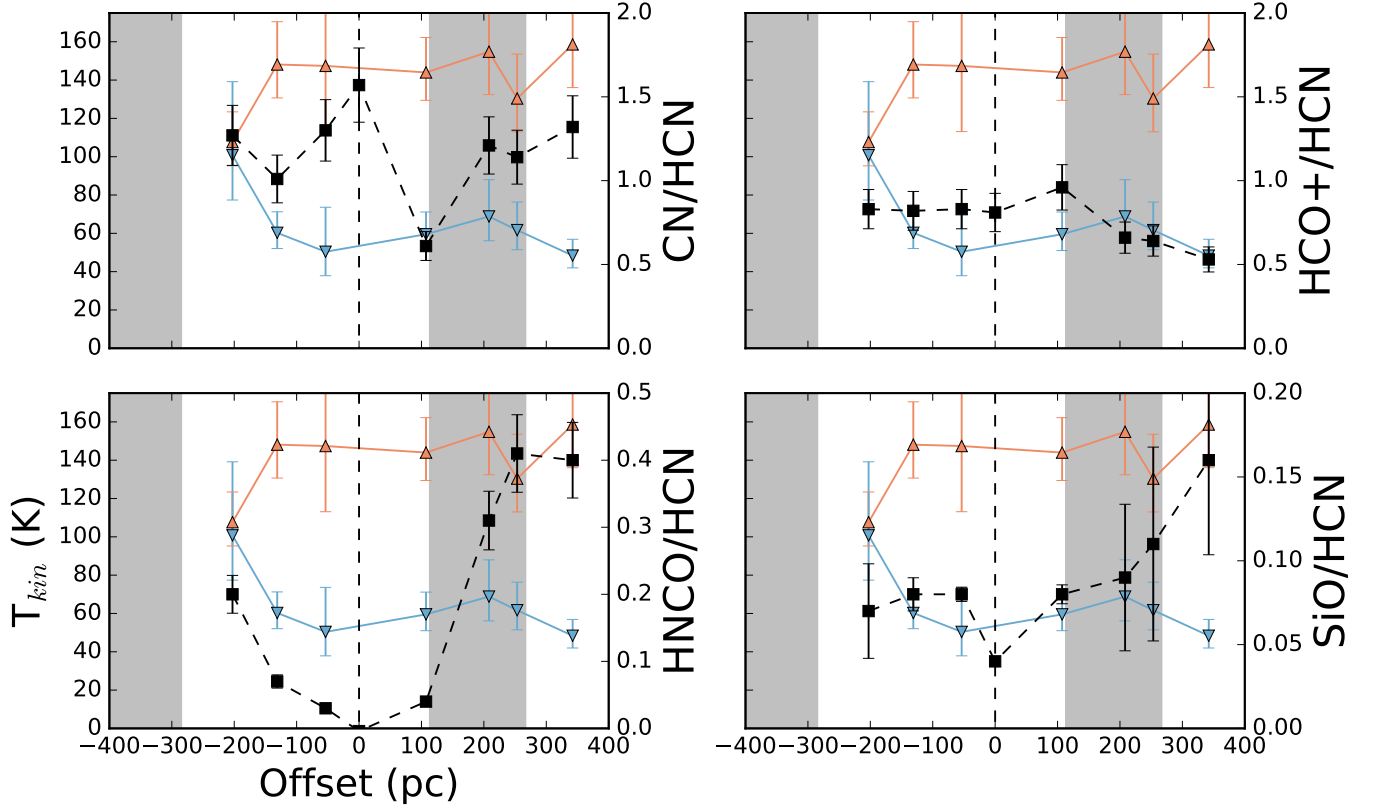


Figure 20. Intensities of molecular tracers relative to HCN from the A1-A7 and C1 locations (dashed lines with black squares). The top row shows the PDR tracer CN (left) and intermediate density tracer HCO⁺ (right) and the bottom row shows weak shock tracer HNCO (left) and strong shock tracer SiO (right). The red triangles and blue inverted triangles with lines are the warm and cool components of the kinetic temperatures we derive from NH₃, respectively. The grey bars represent the diameter and locations of the superbubbles in Sakamoto et al. (2006).

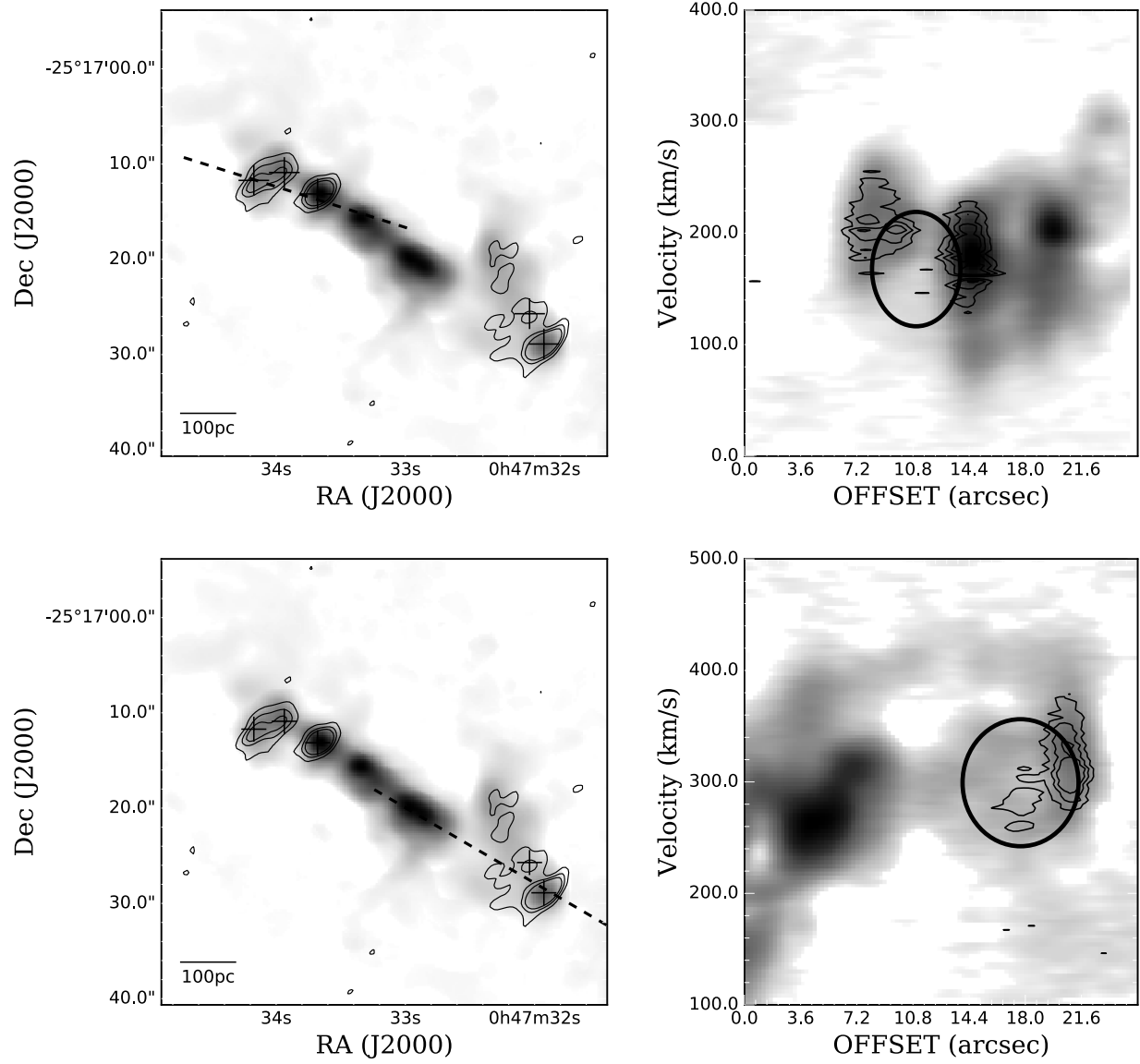


Figure 21. Position-Velocity (PV) cuts through the HCN (grayscale) and 36 GHz methanol maser (3, 6, and 9σ contours shown in black) data cubes. The PV cuts show a few shell-like structures marked with black circles. The methanol masers appear to be concentrated around the edges of the shells.

Table 2. NH₃ Line Parameters From A1-A7

Location	A1	A2	A3	A4	A5	A6	A7
RA (J2000) hh:mm:ss	00:47:34.0	00:47:33.6	00:47:33.3	00:47:32.8	00:47:32.3	00:47:32.2	00:47:31.9
DEC (J2000) ° ' "	-25 17 11.2	-25 17 12.8	-25 17 15.3	-25 17 21.1	-25 17 19.9	-25 17 25.2	-25 17 28.7
Distance from C1* (pc)	202	131	53	107	208	253	342
NH ₃ (1,1)							
$\int T_{mb} d\nu$ (K km s ⁻¹)	48.8±2.1	66.8±2.4	24.6±2.0	57.2±2.2	61.0±3.0	62.4±2.6	59.3±2.3
V_{LSRK} (km s ⁻¹)	200.1±1.8	172.8±1.4	62.8±2.1	278.2±0.1	313.2±2.3	294.5±1.9	299.6±1.4
V_{FWHM} (km s ⁻¹)	83.6±4.2	80.8±3.5	54.2±5.0	65.3±3.2	95.2±6.0	90.0±4.3	74.9±3.5
T_{mb} (K)	0.55±0.08	0.78±0.09	0.43±0.09	0.81±0.09	0.60±0.10	0.65±0.09	0.74±0.09
NH ₃ (2,2)							
$\int T_{mb} d\nu$ (K km s ⁻¹)	44.4±2.1	49.8±1.9	16.7±1.7	42.4±1.7	48.3±2.1	47.0±2.3	39.3±2.0
V_{LSRK} (km s ⁻¹)	225.4±2.0	198.6±1.4	192.2±2.6	309.5±1.1	336.4±2.0	323.2±2.3	328.5±1.8
V_{FWHM} (km s ⁻¹)	87.1±5.3	73.6±3.3	49.7±5.6	55.1±2.6	89.1±4.6	91.4±5.1	74.3±4.4
T_{mb} (K)	0.45±0.08	0.64±0.08	0.32±0.09	0.72±0.08	0.51±0.08	0.48±0.08	0.50±0.08
NH ₃ (3,3)							
$\int T_{mb} d\nu$ (K km s ⁻¹)	74.0±12.1	132.0±2.3	125.5±3.2	126.9±2.3	83.1±2.4	89.9±2.5	80.9±1.6
V_{LSRK} (km s ⁻¹)	204.9±0.8	176.6±0.6	176.2±0.8	283.9±0.5	316.6±1.4	287.9±1.3	308.5±0.6
V_{FWHM} (km s ⁻¹)	68.8±2.0	74.4±1.4	63.7±2.0	61.5±1.4	103.5±3.7	93.7±3.1	66.1±1.6
T_{mb} (K)	1.01±0.07	1.39±0.08	1.85±0.14	1.94±0.10	0.78±0.08	0.90±0.09	1.15±0.07
NH ₃ (4,4)							
$\int T_{mb} d\nu$ (K km s ⁻¹)	15.0±2.1	23.9±1.9	8.0±1.4	19.8±1.3	24.1±2.3	20.0±2.2	20.1±1.7
V_{LSRK} (km s ⁻¹)	199.0±3.7	176.9±2.8	166.5±3.6	286.7±1.6	301.9±5.1	300.3±4.5	310.0±2.8
V_{FWHM} (km s ⁻¹)	59.5±8.6	70.5±6.4	36.5±6.6	44.5±3.3	125.4±13.7	82.4±10.4	64.8±6.2
T_{mb} (K)	0.24±0.09	0.32±0.08	0.21±0.08	0.41±0.07	0.17±0.07	0.23±0.08	0.29±0.09
NH ₃ (5,5)							
$\int T_{mb} d\nu$ (K km s ⁻¹)	12.1±2.4	11.0±1.3	5.2±1.3	16.9±1.8	15.0±2.5	13.2±2.2	11.2±1.5
V_{LSRK} (km s ⁻¹)	195.9±6.1	164.5±2.5	168.3±3.7	281.4±2.7	316.1±7.3	285.6±8.3	294.2±2.4
V_{FWHM} (km s ⁻¹)	71.5±19.2	40.9±5.2	29.0±7.7	53.9±7.6	91.2±19.2	103.5±19.6	36.5±5.1
T_{mb} (K)	0.15±0.08	0.25±0.08	0.17±0.09	0.29±0.08	0.15±0.09	0.12±0.07	0.28±0.09
Rotation Temperatures $T_{JJ'}$							
T_{12} (K)	46 ⁺⁵ ₋₄	37 ⁺² ₋₂	34 ⁺⁶ ₋₄	37 ⁺³ ₋₃	39 ⁺⁴ ₋₃	38 ⁺³ ₋₃	34 ⁺² ₋₂
T_{24} (K)	72 ⁺⁷ ₋₆	89 ⁺⁷ ₋₆	89 ⁺¹⁸ ₋₁₃	87 ⁺⁶ ₋₆	91 ⁺⁹ ₋₈	82 ⁺⁸ ₋₈	93 ⁺⁹ ₋₈
T_{45} (K)	202 ⁺⁴⁰³ ₋₈₄	91 ⁺²¹ ₋₁₅	143 ⁺²¹³ ₋₅₅	226 ⁺¹⁵¹ ₋₆₇	198 ⁺⁶⁹ ₋₃₅	140 ⁺⁹⁵ ₋₄₂	112 ⁺³⁷ ₋₂₃
Kinetic Temperatures $T_{KinJJ'}$							
T_{Kin12} (K)	99 ⁺³⁸ ₋₂₃	60 ⁺¹¹ ₋₈	50 ⁺²³ ₋₁₂	59 ⁺¹¹ ₋₈	68 ⁺¹⁹ ₋₁₂	62 ⁺¹⁵ ₋₁₀	48 ⁺⁹ ₋₆
T_{Kin24} (K)	107 ⁺¹⁵ ₋₁₂	148 ⁺²² ₋₁₁	147 ⁺⁶² ₋₃₄	143 ⁺¹⁸ ₋₁₅	154 ⁺³⁰ ₋₂₂	130 ⁺²³ ₋₁₇	158 ⁺³¹ ₋₂₃

Table 2 continued

Table 2 (*continued*)

Location	A1	A2	A3	A4	A5	A6	A7
RA (J2000) hh:mm:ss	00:47:34.0	00:47:33.6	00:47:33.3	00:47:32.8	00:47:32.3	00:47:32.2	00:47:31.9
DEC (J2000) ° ' "	-25 17 11.2	-25 17 12.8	-25 17 15.3	-25 17 21.1	-25 17 19.9	-25 17 25.2	-25 17 28.7
Distance from C1* (pc)	202	131	53	107	208	253	342
T_{Kin45} (K)	229^{+460}_{-96}	103^{+24}_{-17}	162^{+243}_{-64}	257^{+173}_{-76}	145^{+79}_{-40}	159^{+108}_{-48}	126^{+43}_{-27}

* Right Ascension 00h 47m 33.160s Declination -25° 17' 17.118''

Table 3. Line Parameters Towards C1

NH ₃ (J,K)	$\int T_{mb} d\nu$ (K km s ⁻¹)	V_{LSRK} (km s ⁻¹)	V_{FWHM} (km s ⁻¹)	T_{mb} (K)
Absorption				
NH ₃ (1,1)	-8.1±1.5	223.3±3.4	32.3±6.9	-0.23±0.10
NH ₃ (2,2)	-17.5±1.7	247.7±2.6	49.7±6.6	-0.33±0.08
NH ₃ (4,4)	-10.7±2.4	223.8±6.9	60.0±16.3	-0.17±0.11
NH ₃ (5,5)	-6.8±1.3	218.7±2.9	29.4±6.1	-0.22±0.09
Emission				
NH ₃ (3,3)a	48.6±5.1	171.1±1.1	55.1±3.2	0.82±0.09
NH ₃ (3,3)b	86.7±6.2	256.6±4.5	129.6±9.5	0.63±0.09

Table 4. NH₃ (9,9) Line Parameters at A3

$\int T_{mb} d\nu$ (K km s ⁻¹)	6.9±1.2
V_{LSRK} (km s ⁻¹)	164.7±3.5
V_{FWHM} (km s ⁻¹)	38.1±6.7
T_{mb} (K)	0.17±0.07

Table 5. H₂O Maser Candidates

RA (J2000) hh:mm:ss	Dec(J2000) ° ' "	Velocity Component	$\int T_{mb} d\nu$ (K km s ⁻¹)	V_{LSRK} (km s ⁻¹)	V_{FWHM} (km s ⁻¹)	T_{mb} (K)	Luminosity L_{\odot}
W1							

Table 5 continued

Table 5 (*continued*)

RA (J2000) hh:mm:ss	Dec(J2000) ° ' "	Velocity Component	$\int T_{mb}d\nu$ (K km s ⁻¹)	V_{LSRK} (km s ⁻¹)	V_{FWHM} (km s ⁻¹)	T_{mb} (K)	Luminosity L_{\odot}
00:47:33.1	-25 17 16.9	a	214.9±3.5	109.1±0.3	42.0±0.9	4.7±0.2	0.667
		b	6.2±1.1	27.0±0.4	3.5±0.5	1.7±0.2	0.019
		c	5.5±0.1	21.0	3.5*	1.6±0.2	0.017
W2							
00:47:33.0	-25 17 19.0		25.7±2.7	233.6	107.2±14.0	0.2±0.09	0.080
W3							
00:47:32.8	-25 17 20.7		7.4±0.5	303.6±1.4	3.5±1.1	2.01±0.10	0.023

* unresolved, V_{FWHM} is an upper limit

Table 6. CH₃OH Maser Candidates

RA(J2000) hh:mm:ss	Dec(J2000) ° ' "	Velocity Component	$\int T_{mb} d\nu$ (K km s ⁻¹)	V_{LSRK} (km s ⁻¹)	V_{FWHM} (km s ⁻¹)	T_{mb} (K)	Luminosity L_{\odot}
M1							
00:47:34.1	-25 17 11.7		1.38±0.07	202.0±0.3	49.2±3.1	0.026±0.005	0.63
M2							
00:47:33.9	-25 17 10.8		1.41±0.07	195.4±0.8	32.2±2.3	0.040±0.006	0.65
M3							
00:47:33.7	-25 17 13.1		3.59±0.14	165.9±1.7	85.8±4.4	0.039±0.008	1.63
M4							
00:47:31.9	-25 17 28.9		3.09±0.18	294.1±2.6	84.3±5.6	0.035±0.005	1.42
M5							
00:47:32.0	-25 17 25.7	a	2.19±0.89	294.3±3.0	35.7±4.8	0.056±0.005	1.01
		b	2.33±0.96	331.6±10.2	54.5±16.9	0.041±0.005	1.06

Table 7. NH₃ LVG Best Fit Values

Location	A1	A2	A3	A4	A5	A6	A7

Table 7 continued

Table 7 (*continued*)

Location	A1	A2	A3	A4	A5	A6	A7
$\text{NH}_3(1,1)/\text{NH}_3(2,2)$							
T_{Kin} (K)	117 \pm 135	69 \pm 24	54 \pm 27	69 \pm 24	81 \pm 41	72 \pm 27	57 \pm 18
$\text{NH}_3(2,2)/\text{NH}_3(4,4)$							
T_{Kin} (K)	111 \pm 24	156 \pm 39	165 \pm 75	150 \pm 33	165 \pm 48	108 \pm 24	162 \pm 42

NOTE—This table reports the median temperatures of the best fit LVG model to the data. The uncertainty on the kinetic temperature fit are asymmetric, therefore uncertainty reported here is the greater 1σ deviation from the best fit.

REFERENCES

- Alonso-Herrero, A., Rieke, G. H., Rieke, M. J., & Kelly, D. M. 2003, *AJ*, 125, 1210
- Bolatto, A. D., Warren, S. R., Leroy, A. K., et al. 2013, *Nature*, 499, 450
- Brunthaler, A., Castangia, P., Tarchi, A., et al. 2009, *A&A*, 497, 103
- Caswell, J. L., Breen, S. L., & Ellingsen, S. P. 2011, *MNRAS*, 410, 1283
- Cheung, A. C., Rank, D. M., Townes, C. H., Thornton, D. D., & Welch, W. J. 1968, *Physical Review Letters*, 21, 1701
- Claussen, M. J., Wilking, B. A., Benson, P. J., et al. 1996, *ApJS*, 106, 111
- Claussen, M. J., Goss, W. M., Frail, D. A., & Seta, M. 1999, *AJ*, 117, 1387
- Crain, R. A., Schaye, J., Bower, R. G., et al. 2015, *MNRAS*, 450, 1937
- Dale, D. A., Cohen, S. A., Johnson, L. C., et al. 2009, *ApJ*, 703, 517
- Ellingsen, S. P., Chen, X., Qiao, H.-H., et al. 2014, *ApJL*, 790, L28
- Ellingsen, S. P., Sobolev, A. M., Cragg, D. M., & Godfrey, P. D. 2012, *ApJL*, 759, L5
- Felli, M., Brand, J., Cesaroni, R., et al. 2007, *A&A*, 476, 373
- Fuente, A., Martin-Pintado, J., Cernicharo, J., & Bachiller, R. 1993, *A&A*, 276, 473
- Gao, Y., & Solomon, P. M. 2004, *ApJ*, 606, 271
- García-Burillo, S., Martín-Pintado, J., Fuente, A., & Neri, R. 2000, *A&A*, 355, 499
- Goddi, C., & Moscadelli, L. 2006, *A&A*, 447, 577
- Goddi, C., Henkel, C., Zhang, Q., Zapata, L., & Wilson, T. L. 2015, *A&A*, 573, A109
- Haas, M. R., Schaye, J., Booth, C. M., et al. 2013, *MNRAS*, 435, 2931
- Hartmann, L., Ballesteros-Paredes, J., & Bergin, E. A. 2001, *ApJ*, 562, 852
- Henkel, C., Mauersberger, R., Peck, A. B., Falcke, H., & Hagiwara, Y. 2000, *A&A*, 361, L45
- Henkel, C., Tarchi, A., Menten, K. M., & Peck, A. B. 2004, *A&A*, 414, 117
- Ho, P. T. P., & Townes, C. H. 1983, *ARA&A*, 21, 239
- Hopkins, P. F., Kereš, D., Oñorbe, J., et al. 2014, *MNRAS*, 445, 581
- Hopkins, P. F., Quataert, E., & Murray, N. 2011, *MNRAS*, 417, 950
- Hopkins, P. F., Quataert, E., & Murray, N. 2012, *MNRAS*, 421, 3488
- Huettemeister, S., Wilson, T. L., Mauersberger, R., et al. 1995, *A&A*, 294, 667
- Kauffmann, G., Colberg, J. M., Diaferio, A., & White, S. D. M. 1999, *MNRAS*, 303, 188
- Kepley, A. A., Chomiuk, L., Johnson, K. E., et al. 2011, *ApJL*, 739, L24
- Krumholz, M. R., Klein, R. I., & McKee, C. F. 2011, *ApJ*, 740, 74
- Lebrón, M., Mangum, J. G., Mauersberger, R., et al. 2011, *A&A*, 534, A56
- Leroy, A. K., Bolatto, A. D., Ostriker, E. C., et al. 2015, *ApJ*, 801, 25
- Lo, K. Y. 2005, *ARA&A*, 43, 625
- Mangum, J. G., Darling, J., Henkel, C., et al. 2013, *ApJ*, 779, 33
- McCormick, A., Veilleux, S., & Rupke, D. S. N. 2013, *ApJ*, 774, 126
- McEwen, B. C., Pihlström, Y. M., & Sjouwerman, L. O. 2014, *ApJ*, 793, 133
- McEwen, B. C., Pihlström, Y. M., & Sjouwerman, L. O. 2016, *ApJ*, 826, 189
- McMullin, J. P., Waters, B., Schiebel, D., Young, W., & Golap, K. 2007, *Astronomical Data Analysis Software and Systems XVI*, 376, 127
- Meier, D. S., & Turner, J. L. 2005, *ApJ*, 618, 259
- Meier, D. S., & Turner, J. L. 2012, *ApJ*, 755, 104
- Meier, D. S., Walter, F., Bolatto, A. D., et al. 2015, *ApJ*, 801, 63
- Mills, E. A. C., & Morris, M. R. 2013, *ApJ*, 772, 105
- Miyamoto, Y., Nakai, N., Seta, M., et al. 2015, *PASJ*, 67, 5
- Murray, N., Quataert, E., & Thompson, T. A. 2010, *ApJ*, 709, 191
- Okamoto, T., Eke, V. R., Frenk, C. S., & Jenkins, A. 2005, *MNRAS*, 363, 1299
- Ott, J., Henkel, C., Braatz, J. A., & Weiß, A. 2011, *ApJ*, 742, 95
- Ott, J., Weiss, A., Henkel, C., & Walter, F. 2005, *ApJ*, 629, 767
- Palagi, F., Cesaroni, R., Comoretto, G., Felli, M., & Natale, V. 1993, *A&AS*, 101, 153
- Peck, A. B., Henkel, C., Ulvestad, J. S., et al. 2003, *ApJ*, 590, 149
- Perley, R. A., & Butler, B. J. 2013, *ApJS*, 206, 16
- Pence, W. D. 1980, *ApJ*, 239, 54

- Pratap, P., Shute, P. A., Keane, T. C., Battersby, C., & Sterling, S. 2008, *AJ*, 135, 1718
- Radburn-Smith, D. J., de Jong, R. S., Seth, A. C., et al. 2011, *ApJS*, 195, 18
- Reid, M. J., Braatz, J. A., Condon, J. J., et al. 2009, *ApJ*, 695, 287
- Rodríguez-Franco, A., Martín-Pintado, J., & Fuente, A. 1998, *A&A*, 329, 1097
- Rosenberg, M. J. F., Kazandjian, M. V., van der Werf, P. P., et al. 2014, *A&A*, 564, A126
- Sakamoto, K., Ho, P. T. P., Iono, D., et al. 2006, *ApJ*, 636, 685
- Sakamoto, K., Mao, R.-Q., Matsushita, S., et al. 2011, *ApJ*, 735, 19
- Schöier, F. L., van der Tak, F. F. S., van Dishoeck, E. F., & Black, J. H. 2005, *A&A*, 432, 369
- Strickland, D. K., Heckman, T. M., Weaver, K. A., Hoopes, C. G., & Dahlem, M. 2002, *ApJ*, 568, 689
- Takano, S., Hofner, P., Winnewisser, G., Nakai, N., & Kawaguchi, K. 2005, *PASJ*, 57, 549
- Tarchi, A. 2012, *IAU Symposium*, 287, 323
- Turner, B. E. 1995, *ApJ*, 449, 635
- Turner, J. L., & Ho, P. T. P. 1985, *ApJL*, 299, L77
- Ulvestad, J. S., & Antonucci, R. R. J. 1997, *ApJ*, 488, 621
- Van der Tak, F.F.S., Black, J.H., Schier, F.L., Jansen, D.J., van Dishoeck, E.F., 2007, *A&A*, 468, 627-635
- Vázquez-Semadeni, E., Colín, P., Gómez, G. C., Ballesteros-Paredes, J., & Watson, A. W. 2010, *ApJ*, 715, 1302
- Walmsley, C. M., & Ungerechts, H. 1983, *A&A*, 122, 164
- Watson, A. M., Gallagher, J. S., III, Holtzman, J. A., et al. 1996, *AJ*, 112, 534
- Westmoquette, M. S., Smith, L. J., & Gallagher, J. S., III 2011, *MNRAS*, 414, 3719
- Whiting, A. B. 1999, *AJ*, 117, 202
- Wilson, T. L., & Mauersberger, R. 1990, *A&A*, 239, 305
- Yamagishi, M., Kaneda, H., Ishihara, D., et al. 2010, *PASJ*, 62, 1085
- Yusef-Zadeh, F., Cotton, W., Viti, S., Wardle, M., & Royster, M. 2013, *ApJL*, 764, L19